38 Taylor Dispersion in Sample Preconcentration Methods

Rajiv Bharadwaj, David E. Huber, Tarun Khurana, and Juan G. Santiago

CONTENTS

38.1 INTRODUCTION

Sample preconcentration methods, including stacking and focusing techniques, enable high-sensitivity detection by increasing analyte ion concentration. Sample preconcentration also leads to a decrease in the axial dimension of sample plugs (i.e., peak widths) and this can improve resolution in electrophoretic separations. In this chapter, we describe the basic principles and limitations of electrokinetic sample stacking and focusing techniques. We highlight the importance of Taylor dispersion in determining the efficiency of preconcentration methods. Sample preconcentration techniques can be broadly classified into two types:

1. In an increase in sample ion concentration occurs due to a local decrease in the magnitude of the drift velocity of an ion. For drift velocity vector field $\bar{v}_d$, stacking occurs when

locally $\nabla \cdot \bar{v}_d < 0$. These gradients are typically limited to a small region relative to the length of a separation channel. Ions enter the region, are stacked, leave the region, and subsequently disperse and decrease in concentration. After stacking, peak (spatial) variance tends to grow linearly in time. Stacking includes field-amplified sample stacking (FASS) and its derivative techniques.

2. In focusing, the condition $\nabla \cdot \bar{v}_d < 0$ is typically satisfied throughout a large extent of the channel and there is, additionally, a focal point, $\bar{x}_{foc}$ (or focal region), for the solute. There is a reference frame where the continuous vector field $\bar{v}_d$ changes sign at $\bar{x}_{foc}$. In this frame, the opposing signs of $\bar{v}_d$ drive the initially widely distributed sample to $\bar{x}_{foc}$, where sample ions accumulate. For a finite amount of sample, sample peak width reaches a steady-state value determined by the opposing effects of the $\bar{v}_d$ gradient and dispersion. Focusing includes isoelectric focusing (IEF) and thermal gradient focusing (TGF) where $\bar{x}_{foc}$ is fixed in space; and also includes isotachophoresis (ITP) where $\bar{x}_{foc}$ propagates at a wave speed set by the bulk flow and the ion mobilities in the system.

Leveraging heterogeneous buffer systems to effect changes in sample drift velocity is a common feature of electrophoretic preconcentration techniques. The sample and background electrolyte (BGE) can differ in ionic strength and ionic makeup (e.g., ion mobility or valence). The theoretical concentration enhancement of most of these techniques has been well known for many decades. For example, the maximum concentration enhancement in FASS is predicted to be equal to the ratio of the (relatively high) conductivity of the BGE to the (relatively low) conductivity of the sample solution. This ratio determines the low-to-high analyte drift velocity ratio. In ITP, the theoretical drift velocity ratio and associated prediction of concentration enhancement is a function of the leading ion concentration and various ionic mobilities. Several numerical simulation tools that can predict the concentration enhancement in various electrophoretic preconcentration techniques are available. One fairly comprehensive and useful simulation tools is Simul, which is available free download on the Web [1]. Simul solves one-dimensional multispecies electromigration–diffusion phenomena (e.g., for electromigration in long thin tubes of constant area). The code includes ionization equilibria of weak electrolytes, calculation of local pH fields, and the dependence of ionic mobilities on ionic strength and pH. Given initial conditions and ion information (e.g., fully ionized mobility, pK_a values, diffusivity), the code predicts the evolution of ionic species in the presence of an electric field. Simul is, however, limited to one dimension and does not include flow-induced dispersion caused by nonuniform electroosmosis or body forces due to conductivity gradients.

In practice, both molecular diffusion and advective dispersion (i.e., Taylor dispersion [2]) limit the achievable concentration enhancement of preconcentration techniques. In some techniques, such as TGF, an external-pressure-driven velocity field is integral to the focusing effect and dispersive effects are inherent in the system. In other techniques such as FASS, external-pressure-driven flows are minimal (e.g., due to unwanted hydrostatic pressure heads in end-channel reservoirs). However, despite efforts to suppress electroosmotic flow (EOF), electrophoresis in capillaries is typically accompanied by at least trace EOF. The heterogenous nature of buffers creates gradients in EOF mobility. These heterogeneities include ion density and ion mobilities and may also include temperature gradients, valence (via chemical reactions), and perhaps permittivity and viscosity. More importantly, variations in local ionic conductivity (and local permittivity) affect strong variations in local electric field. Both these effects (gradients in EOF mobility and gradients in field) create nonuniform EOF that leads to the generation of internal pressure gradients. Secondary flows generated by these pressure gradients tend to disperse analyte plugs and reduce the preconcentration effect.

In this chapter, we will identify the role and the scaling of dispersive effects in determining the ultimate limits of sample preconcentration techniques. Where possible, we will offer simple quantitative theory for estimating the effects of dispersion, and in all cases we will provide scaling arguments that can help guide empirical optimization of preconcentration techniques. First, we will

explain the basic physics of Taylor dispersion and provide reduced order models to qualitatively and quantitatively describe it. Second, we will present simple relations to estimate the importance of Taylor dispersion in relation to other peak broadening mechanisms in capillary electrophoresis (CE) systems. These relations are useful in, for example, empirically identifying optima in applied field and conductivity ratios. Finally, we will briefly describe three examples of preconcentration techniques as instructive "case studies" in which dispersion plays an important role in determining concentration enhancement.

38.2 BACKGROUND

Dispersion, the tendency for ordered molecules to decrease gradients and local concentration, is caused by both molecular diffusion and nonuniform bulk liquid motion. High dispersion rates may be advantageous for mixing and chemical reactions, but are undesirable in separation and purification applications. For separations, minimizing dispersion improves resolution and sensitivity [3] and yields improved dynamics for concentration and purification [4]. As a consequence, the physical processes that lead to dispersion have been a subject of intense interest for more than a century. In recent years, the development of the concept of the micro-total analysis system (μTAS) or "labs on a chip" has motivated further exploration of dispersion in microchannel flows.

In the field of CE, researchers are most familiar with dispersion caused by molecular diffusion and Taylor dispersion [2]. In 1953, G. I. Taylor demonstrated that, under certain conditions, the cross-sectional average of the unsteady, three-dimensional concentration field within a channel evolves as a one-dimensional convective–diffusion equation with a coefficient analogous to a modified diffusivity. Here, the advective dispersion in the axial direction is balanced by spanwise and depthwise (e.g., radial in a cylindrical tube) diffusion, causing peak variance to increase linearly in time, with the characteristic slope determined by an effective dispersion coefficient. Taylor further demonstrated that given enough time, theoretically, all solute plugs flowing within a channel ultimately reach this limit. Subsequently, Aris [5] proved that the (now named) Taylor regime could be unified with the pure diffusive regime by using an effective dispersion coefficient, which was the sum of the molecular diffusivity and the Taylor dispersion coefficient. The effective dispersion concept has proved to be extremely useful and has been extended to other geometries [6], generalized using alternative analyses [7,8], and extended to apply to EOF [9] and electrophoresis in nanochannels [10,11].

38.3 THEORETICAL ASPECTS

The nonuniform velocity distribution over the cross section of a capillary or a microchannel leads to distortion of the sample plug. This velocity-induced distortion generates a radial concentration gradient of the analyte. Molecular diffusion acts to reduce this radial concentration gradient. The two effects in tandem determine the effective dispersion rate of the sample plug. The increase in variance can be quantified in terms of an effective dispersion coefficient, D_{eff}. In this section, we will describe the details of calculating this effective diffusion coefficient for a sample velocity profile. This section is targeted at readers who may want to understand the mathematical details behind calculation of D_{eff}. Practitioners who are not interested in these details may skip to the next section without loss of continuity. The next section describes simple relations to estimate the role of dispersion in peak broadening in CE.

38.3.1 Taylor Dispersion Analysis via Area Averaging

We derive the Taylor dispersion equation using an area averaging approach as described by Stone and Brenner [8]. We consider axisymmetric flow in a cylindrical capillary of radius "a," but will later discuss the application of these principles to other cross sections (such as typical wet etched

"D" profiles). We consider a nonuniform (in x) drift velocity to account for electrophoresis, and the scaling of streamwise coordinates by a characteristic length $U_p t_c$, where U_p is the magnitude of the deviation of axial velocity from the area-averaged velocity and t_c is the characteristic time for stacking or focusing. This approach can be applied to stacking and focusing. The following equations describe the convective dispersion of a charged species in a parabolic velocity field:

$$\begin{aligned}
&\frac{\partial C_i}{\partial t} + \frac{\partial}{\partial x}\left(u_{ti}\left(x,r\right)C_i\right) = D_i\left(\frac{1}{r}\frac{\partial}{\partial r}\left(r\frac{\partial C_i}{\partial r}\right) + \frac{\partial^2 C_i}{\partial x^2}\right); \quad i = 1:N,\\
&\frac{\partial C_i}{\partial r} = 0 \quad \text{at } r = a, 0,
\end{aligned} \tag{38.1}$$

where C_i is the concentration of a dilute and, in general, charged solute of interest. In general electrokinetic flow physics, applied electric fields couple with conductivity gradients and lead to the generation of net charge in the bulk liquid. However, this charge density is negligible compared to the total background ion concentration. We can, therefore, assume that the solution is approximately electrically neutral everywhere outside of the electrical double layer, so that $\sum_{i=1}^{N} z_i C_i \approx 0$, where z_i is the valence. This approximation is discussed in detail elsewhere [12–14].

In Equation 38.1, we have made the typical "nearly parallel flow" approximation common in lubrication analysis that the flow is nearly parallel to the axis in this long thin tube [15]. This approximation holds as long as axial gradients in electroosmotic mobility and conductivity scale is $1/\sigma$, where the characteristic plug width of the solute, σ, is such that $\sigma \gg a$. This condition is commonly met in sample stacking and focusing techniques, although it may not be met in, for example, high field regimes of ITP in the so-called peak mode. This and other limitations are discussed later.

We consider the velocity field bounded by a cylindrical slip surface, which excludes a thin electric double layer (EDL) [16]. The velocity scale u_t includes the effects of local pressure gradients, electroosmosis, and electrophoresis and can be expressed as follows:

$$u_{ti}(x,r,t) \cong u_p(x,r,t) + U_{\text{eph},i}(x,t) + U_{\text{eof}}(x,t), \tag{38.2}$$

where $u_p(x,r,t)$ is the axial velocity component due to a local pressure gradient, $\partial p(x,t)/\partial x$, and equal to $-a^2(\partial p/\partial x)(1 - r^2/a^2)/4\eta$, where η is dynamic viscosity.

$U_{\text{eph},i}(x,t)$ is an axial electrophoretic drift due to an approximately purely axial electric field, $E(x,t)$, and can be written as $z_i F \mu_{\text{eph},i} E(x,t)$, where z_i, $\mu_{\text{eph},i}$, and F are the valence, electrophoretic mobility, and Faraday's constant [12]. $U_{\text{eof}}(x,t)$ is the (exactly axial) velocity component due to electroosmosis, which can be expressed as $zF\mu_{\text{eof}}E(x,t)$, where μ_{eof} is electroosmotic mobility and $E(x,t)$ is the axial field component at the slip plane (near the wall). We also consider changes slow enough such that fluid inertia and charge relaxation are negligible. See Storey et al. [17] and Lin et al. [18] for more detailed discussion of quasi-steady electromigration, electroosmosis, and pressure-driven flow in long thin channels.

We define $U_e(x,t) = U_{\text{eph},i}(x,t) + U_{\text{eof}}(x,t)$ as the sum of the electroosmotic and approximately parallel electrophoretic velocities. Note that $\nabla\cdot(U_{\text{eof}} + u_p) = \partial(U_{\text{eof}} + u_p)/\partial x = 0$. The convective diffusion equation then becomes

$$\frac{\partial C_i}{\partial t} + (U_{e,i} + u_p)\frac{\partial C_i}{\partial x} + \frac{\partial U_{\text{eph},i}}{\partial x}C_i = D_i\left(\frac{1}{r}\frac{\partial}{\partial r}\left(r\frac{\partial C_i}{\partial r}\right) + \frac{\partial^2 C_i}{\partial x^2}\right). \tag{38.3}$$

The dependent variables are expressed in terms of cross-sectional averages and deviations:

$$\begin{aligned}
C_i(x,r,t) &= \langle C_i\rangle(x,t) + C_i'(x,r,t),\\
u(x,r,t) &= \langle u_p\rangle(x,t) + \langle U_{e,i}\rangle(x,t) + u_p'(x,r,t) = U_p + U_{e,i} + u_p.
\end{aligned} \tag{38.4}$$

The cross-sectional average is defined as $\langle \cdots \rangle = 1/\pi a^2 \int_0^a 2\pi r(\cdots)\mathrm{d}r$. Note u_p' is $U_p(1-2r^2/a^2)$, where $U_p = -\pi a^4(\partial p/\partial x)/8\eta$ is the bulk (area-averaged) velocity due to pressure gradients. We can interpret primed quantities as describing the concentration field in a frame moving with the area-averaged velocity of the solute. Substituting these definitions into Equation 38.1:

$$\frac{\partial \langle C_i\rangle}{\partial t} + \frac{\partial C_i'}{\partial t} + (U_{e,i} + \langle u_p\rangle)\frac{\partial \langle C_i\rangle}{\partial x} + (U_{e,i} + \langle u_p\rangle)\frac{\partial C_i'}{\partial x} + u_p'\frac{\partial \langle C_i\rangle}{\partial x} + u_p'\frac{\partial C_i'}{\partial x} + \frac{\partial U_{\mathrm{eph},i}}{\partial x}\langle C_i\rangle + \frac{\partial U_{\mathrm{eph},i}}{\partial x}C_i' = D_i\left(\frac{1}{r}\frac{\partial}{\partial r}\left(r\frac{\partial C_i'}{\partial r}\right) + \frac{\partial^2\langle C_i\rangle}{\partial x^2} + \frac{\partial^2 C_i'}{\partial x^2}\right). \tag{38.5}$$

Subject to

$$\frac{\partial C_i'}{\partial r} = 0 \quad \text{at } r = a, 0.$$

Note that $\langle U_{\mathrm{eph},i}\rangle = U_{\mathrm{eph},i}$ and $U'_{\mathrm{eph},i} = 0$. The boundary conditions (BC) reduce to this since $\partial\langle C_i\rangle/\partial r$ is exactly zero by definition, $\langle C_i\rangle$ being only a function of x. Next, we take a cross-sectional average of Equation 38.5:

$$\frac{\partial \langle C_i\rangle}{\partial t} + \underbrace{\left\langle\frac{\partial C_i'}{\partial t}\right\rangle}_{=0 \text{ by def}} + (U_{e,i} + \langle u_p\rangle)\frac{\partial \langle C_i\rangle}{\partial x} + \underbrace{(U_{e,i} + \langle u_p\rangle)\left\langle\frac{\partial C_i'}{\partial x}\right\rangle}_{=0 \text{ by def}} + \underbrace{\left\langle u_p'\right\rangle\frac{\partial\langle C_i\rangle}{\partial x}}_{=0 \text{ by def}}$$
$$+ \left\langle u_p'\frac{\partial C_i'}{\partial x}\right\rangle + \frac{\partial U_{\mathrm{eph},i}}{\partial x}\langle C_i\rangle + \underbrace{\left\langle\frac{\partial U_{\mathrm{eph},i}}{\partial x}C_i'\right\rangle}_{=0 \text{ by def}} = D_i\left(\underbrace{\left\langle\frac{1}{r}\frac{\partial}{\partial r}\left(r\frac{\partial C_i'}{\partial r}\right)\right\rangle}_{\text{evaluate using BC}} + \frac{\partial^2\langle C_i\rangle}{\partial x^2} + \underbrace{\left\langle\frac{\partial^2 C_i'}{\partial x^2}\right\rangle}_{=0 \text{ by def}}\right), \tag{38.6}$$

where the notes "$=0$ by def" and "evaluate using BC" denote a quantity zero by definition and a term that can be evaluated with the BCs. Evaluating the first term on the right-hand side:

$$\left\langle\frac{1}{r}\frac{\partial}{\partial r}\left(r\frac{\partial C_i'}{\partial r}\right)\right\rangle = \frac{1}{\pi a^2}\int_0^a 2\pi\frac{\partial}{\partial r}\left(r\frac{\partial C_i'}{\partial r}\right)\mathrm{d}r = \frac{2}{a^2}\int_0^a \mathrm{d}\left(\mathrm{r}\frac{\partial \mathrm{C_i'}}{\partial \mathrm{r}}\right) = r\left.\frac{\partial C_i'}{\partial r}\right|_a - r\left.\frac{\partial C_i'}{\partial r}\right|_0 = 0.$$

(From BC, $\partial C_i'/\partial r$ is zero at both $r = 0$ and $r = a$.) Collecting nonzero terms in Equation 38.6:

$$\frac{\partial\langle C_i\rangle}{\partial t} + \left(U_{e,i} + \langle u_p\rangle\right)\frac{\partial\langle C_i\rangle}{\partial x^2} + \frac{\partial U_{\mathrm{eph},i}}{\partial x}\langle C_i\rangle = D_i\left(\frac{\partial^2\langle C_i\rangle}{\partial x^2}\right) - \left\langle u_p'\frac{\partial C_i'}{\partial x}\right\rangle. \tag{38.7}$$

The cross-correlation term is placed on the right-hand side as it acts as a source of dispersion (as does diffusion). We now derive an expression for C_i'. To do so, subtract Equation 38.7 from Equation 38.5:

$$\frac{\partial C_i'}{\partial t} + u_p'\frac{\partial\langle C_i\rangle}{\partial x} + \left(U_{e,i} + \langle u_p\rangle\right)\frac{\partial C_i'}{\partial x} + u_p'\frac{\partial C_i'}{\partial x} + \frac{\partial U_{\mathrm{eph},i}}{\partial x}C_i'$$
$$= D_i\left(\frac{1}{r}\frac{\partial}{\partial r}\left(r\frac{\partial C_i'}{\partial r}\right) + \frac{\partial^2 C_i'}{\partial x^2}\right) + \left\langle u_p'\frac{\partial C_i'}{\partial x}\right\rangle. \tag{38.8}$$

Scale the variables as follows: $r^* = r/a$, $x^* = x/\sigma$, $C_i'^* = C_i'/C_{io}'$, $\langle C_i\rangle^* = \langle C_i\rangle/C_{io}$, $t^* = t/t_c$, and $\langle u_p\rangle^* = \langle u_p\rangle/U_p = 1$, $u_p'^* = u_p'/U_p$, and $\langle U_{e,i}\rangle^* = \langle U_{e,i}\rangle/(U_{\text{eph},i}(x,t) + U_{\text{eof}}(x,t)) = 1$. We choose both C_{io}' and C_{io} as we will use the ratio C_{io}'/C_{io} as a smallness parameter in our scaling arguments.

We scale axial gradients using the characteristic width of dispersion σ. For techniques where variance width of the sample plug increases approximately linearly in time, we can interpret σ as the characteristic length scale of advective dispersion, $U_p t_c$. Here, t_c is the time of observation or time between injection and detection. In focusing techniques where solute dispersion length scales reach a steady value, σ is an inherent length scale associated with the focusing stacking dynamics. For example, in ITP stacking or TGF of finite injection volumes, sample widths eventually reach a steady-state value. In these techniques, the axial concentration and velocity gradients of the peak are determined by the interplay between electromigration (which provides the focusing fluxes) and diffusion and dispersion (which limit the amount of stacking). The inherent length scale of dispersion, σ, is then an internal length scale (i.e., determined by the specific condition). For such cases, we will assume $\sigma \gg a$ with the understanding that the analysis is checked for self consistency and is only valid if it indeed predicts long thin solute plugs.

Equation 38.8 can then be written as

$$\left(\frac{C_{o,i}'}{t_c}\right)\frac{\partial C_i^*}{\partial t^*} + \left(\frac{U_p C_{o,i}}{\sigma}\right)u_p'^*\frac{\partial\langle C_i\rangle^*}{\partial x^*} + \left(\frac{C_{o,i}'}{\sigma}\right)(U_p + U_{e,i} + U_p u_p'^*)\frac{\partial C_i^*}{\partial x^*} + \left(\frac{U_p C_{o,i}'}{\sigma}\right)\frac{\partial U_{\text{eph},i}}{\partial x^*}C_i'$$
$$= \left(\frac{D_i C_{o,i}'}{a^2}\right)\left(\frac{1}{r^*}\frac{\partial}{\partial r^*}\left(r^*\frac{\partial C_i^*}{\partial r^*}\right)\right) + \left(\frac{D_i C_{o,i}'}{\sigma^2}\right)\frac{\partial^2 C_i'^*}{\partial x^{*2}} + \left(\frac{U_p C_{o,i}'}{\sigma}\right)\left\langle u_p'^*\frac{\partial C_i'^*}{\partial x^*}\right\rangle. \tag{38.9}$$

Next, multiply this equation by $a^2/(D_i C_{o,i})$.

$$\underbrace{\left(\frac{a^2 C_{o,i}'}{D_i t_c C_{o,i}}\right)}_{\text{order }\varepsilon^2}\frac{\partial C_i'^*}{\partial t^*} + \underbrace{\left(\frac{a^2 U_p}{\sigma D_i}\right)}_{\text{order }\varepsilon}u_p'^*\frac{\partial\langle Ci\rangle^*}{\partial x^*} + \underbrace{\left(\frac{a^2 U_p C_{o,i}'}{\sigma D_i C_{o,i}}\right)}_{\text{order }\varepsilon^2}\left(1 + \frac{U_{e,i}}{U_p} + u_p'^*\right)\frac{\partial C_i'^*}{\partial x^*} + \underbrace{\left(\frac{a^2 Up C_{o.i}'}{\sigma D_i C_{o,i}}\right)}_{\text{order }\varepsilon^2}$$
$$\times\frac{\partial U_{\text{eph},i}'}{\partial x}C_i' = \underbrace{\left(\frac{C_{o,i}'}{C_{o,i}}\right)}_{\text{order }\varepsilon}\left(\frac{1}{r^*}\frac{\partial}{\partial r^*}\left(r^*\frac{\partial C_i'^*}{\partial r^*}\right)\right) + \underbrace{\left(\frac{a^2 C_{o,i}'}{\sigma D_i C_{o,i}}\right)}_{\text{order }\varepsilon^2}\frac{\partial^2 C_i'^*}{\partial x^{*2}} + \underbrace{\left(\frac{a^2 U_p C_{o,i}'}{\sigma D_i C_{o,i}}\right)}_{\text{order }\varepsilon^2}\left\langle u_p'^*\frac{\partial C_i'^*}{\partial x^*}\right\rangle. \tag{38.10}$$

The notes below the various terms denote the order of magnitude. Of interest are the long times relative to streamwise transport so that $t_c \gg a^2/D_i$. In other words, the plug is long compared to the radius of the capillary such that $\sigma \gg a$ and the smallness parameter, ε, is

$$\varepsilon \sim \left(\frac{a}{\sigma}\right)^2 \sim \frac{a^2}{D_i t_c} \ll 1.$$

For the third term on the left-hand side, we assume that the displacement time, $\sigma/(U_p + U_{e,i}(x))$, is much longer than the radial diffusion time, a^2/D_i. For TGF, $U_p + U_{e,i}(x) = 0$ and the term in question is zero. For FASS and ITP, the solute plug velocity, $U_p + U_{e,i}$, is finite and this assumption implies the diffusion time, a^2/D_i, must be smaller than the time required for the plug to move a characteristic distance σ. This condition should hold for FASS where typically σ is significantly larger than a. For ITP, we will restrict our analysis to the cases where this third term is negligible. In comparing the second and third terms on the left-hand side, we see this assumption allows $[U_p + U_{e,i}]/U_p$ to be somewhat larger than unity (or smaller), but not so large that $[U_p + U_{e,i}]C_{o,i}'/(U_p C_{o,i})$ is order

unity. This seems reasonable for ITP plugs with interface axial lengths, σ, of order a and larger. (The challenges of analyzing Taylor dispersion in ITP are discussed further below.) The current assumptions lead to the following:

$$\left(\frac{a^2 U_p}{\sigma D_i}\right) u_p'^* \frac{\partial \langle C_i\rangle^*}{\partial x^*} \approx \left(\frac{C'_{o,i}}{C_{o,i}}\right)\left(\frac{1}{r^*}\frac{\partial}{\partial r^*}\left(r^*\frac{\partial C_i'^*}{\partial r^*}\right)\right). \tag{38.11}$$

Or, in dimensional form:

$$u_p' \frac{\partial \langle C_i\rangle}{\partial x} \approx D_i\left(\frac{1}{r}\frac{\partial}{\partial r}\left(r\frac{\partial C_i'}{\partial r}\right)\right). \tag{38.12}$$

Perturbations in the axial velocity must be balanced by radial diffusion. Substituting for u_p'

$$U_p\left(1-\frac{2r^2}{a^2}\right)\frac{\partial \langle C_i\rangle}{\partial x} \approx D_i\left(\frac{1}{r}\frac{\partial}{\partial r}\left(r\frac{\partial C_i'}{\partial r}\right)\right).$$

Multiply both sides by r and integrate in r

$$U_p \frac{\partial \langle C_i\rangle}{\partial x}\left(\frac{r^2}{2}-\frac{r^4}{2a^2}\right) \approx D_i\left(r\frac{\partial C_i'}{\partial r}\right) + C_1.$$

Apply BC at $r = a$: $C_1 = 0$. Divide both sides by r (and D) and integrate again:

$$C_i'(r,x,t) = C_i'(0,x,t) + \frac{U_p(x,t)\,a^2}{4D_i}\frac{\partial \langle C_i\rangle}{\partial x}\left[\frac{r^2}{a^2}-\frac{r^4}{2a^4}\right]. \tag{38.13}$$

where $C_i'(0,x,t)$ is the constant of integration obtained from the BC at $r = 0$. Now, we can evaluate the cross term in Equation 38.7. Take the x-derivative of Equation 38.13,

$$\frac{\partial C_i'(r,x,t)}{\partial x} = \frac{\partial C_i'(0,x,t)}{\partial x} + \frac{\partial}{\partial x}\left(U_p\frac{\partial \langle C_i\rangle}{\partial x}\right)\frac{a^2}{4D_i}\left[\frac{r^2}{a^2}-\frac{r^4}{2a^4}\right].$$

multiply this by u' (from Equation 38.4), and integrate over the cross section:

$$\left\langle u'\frac{\partial C_i'}{\partial x}\right\rangle = -\frac{\partial}{\partial x}\left(\frac{a^2U_p^2}{48D_i}\frac{\partial \langle C_i\rangle}{\partial x}\right). \tag{38.14}$$

Substitute this into Equation 38.7, which was the area average of the originally decomposed convective diffusion equation, to yield

$$\frac{\partial \langle C_i\rangle}{\partial t} + (U_{e,i} + \langle u_p\rangle)\frac{\partial \langle C_i\rangle}{\partial x} + \frac{\partial U_{\text{eph},i}}{\partial x}\langle C_i\rangle = D_i\left(\frac{\partial^2 \langle C_i\rangle}{\partial x^2}\right) + \frac{\partial}{\partial x}\left(\frac{a^2U_p^2}{48D_i}\frac{\partial \langle C_i\rangle}{\partial x}\right). \tag{38.15}$$

To review, the main assumptions are that the velocity and electric fields are nearly parallel and that $a^2/(D_i t_{\text{obs}}) \ll 1$ and $a/\sigma \ll 1$.

We rewrite Equation 38.15 as

$$\frac{\partial \langle C_i\rangle}{\partial t} + (U_{\text{eph},i} + U_{\text{eof}} + U_p)\frac{\partial \langle C_i\rangle}{\partial x} + \frac{\partial U_{\text{eph},i}}{\partial x}\langle C_i\rangle = \frac{\partial}{\partial x}\left(D_{\text{eff},i}\frac{\partial \langle C_i\rangle}{\partial x}\right), \tag{38.16}$$

where $D_{\text{eff},i}(x,t) = D_i + a^2 U_p(x,t)^2/(48D_i) = D_i(1 + Pe_i^2/48)$. Here Pe_i is a Peclet number defined as $U_p a/D_i$. We do not know of analytical solutions to the nontrivial cases where $U_{\text{eph},i}$, U_{eof}, and U_p indeed vary in x (as in the case of nonuniform EOF velocities), and so this requires numerical solutions. However, we argue that significant insight can be gleaned from this equation, and this insight is valuable in optimizing sample preconcentration processes.

The previously mentioned equation shows that the area-averaged solute plugs will travel along the capillary with a nonuniform wave velocity of the form $U_{\text{eph},i} + U_{\text{eof}} + U_p$, as expected. The local dispersion coefficient, $D_{\text{eff},i}$, is strictly a function of the pressure-driven flow component, which has nonzero radial gradients, and has the same form as the well-known Taylor–Aris solution [5], but with axial and temporal variations in the dispersion coefficient. The focusing effect of electrophoresis is captured by the electrophoresis term $\langle C_i \rangle \partial U_{\text{eph},i}/\partial x$. This analysis captures the interplay between dispersion and preconcentration forces in electrophoretic stacking methods. $D_{\text{eff},i}$ acts to increase sample plug variance (in the absence of stacking fluxes, variance scales as $D_{\text{eff},i}t$, where t is time). This dispersion is countered by gradients of ion drif velocity that generate a negative value of $\langle C_i \rangle \partial U_{\text{eph},i}/\partial x$. For a positive x-direction electric field, preconcentration (local increase in $\langle C_i \rangle$) occurs for a cation when $U_{\text{eff},i}$ has negative axial gradient, $\partial U_{\text{eph},i}/\partial x < 0$ (and where $\partial U_{\text{eph},i}/\partial x > 0$ for an anion). Opposite signs for $\partial U_{\text{eph},i}/\partial x$ cause so-called electromigration dispersion and associated reductions in $\langle C_i \rangle$ [19]. As described earlier, focusing occurs when we have a frame of reference in which $\partial U_{\text{eph},i}/\partial x$ is accompanied by a change in sign of the electrophoretic velocity, and solute is driven toward this focal point from large regions of the channel. [U_{eof} and U_p cannot cause preconcentration since $\nabla \cdot (U_{\text{eof}} + U_p)$ is identically zero.] The relative strength of stacking and focusing versus dispersion is determined by the relative strength of $\partial U_{\text{eph},i}/\partial x$ and $D_{\text{eff},i}$; more simply, $\partial U_{\text{eph},i}/\partial x$ acts to reduce σ while $D_{\text{eff},i}$ acts to increase it. This balance determines the maximum achievable concentration increase, and can determine the resolution of simultaneous preconcentration and separation. This concept is further developed in the next section.

As mentioned earlier, Taylor-type dispersion analyses have been extended to other geometries including flow in rectangular channels of varying aspect ratio and channels with the characteristic "D" shape of isotropic chemical etching [6,20]. In general, these analyses lead to an effective dispersion coefficient of the form $D(1 + \kappa Pe^2)$, where κ takes into account geometric dependences. Table 38.1 list sample κ values for several flow geometries. This elegant and general form of the dispersion coefficient implies that the insights gained by the area-averaging are generally applicable to dispersion in a wide range of geometries.

Often, microchannels are etched with finite (and sometimes high) width-to-depth aspect ratios, w/h, with typical values ranging from 2 to 20. For such channels, the time scale for diffusion across

TABLE 38.1
Taylor Dispersion κ Values for Various Cross-sectional Geometries

Cross-Sectional Geometry	κ
Ellipse	$\frac{1}{192}\left(\frac{24 - 24e^2 + 5e^4}{24 - 12e^2}\right)$; $e = \sqrt{1 - d^2/W^2}$; where d and W are the minor and major axes, respectively
Rectangle	$\frac{1}{210}\left(\frac{8.5W^2}{d^2 + 2.4dW + W^2}\right)$; where d and W are the channel depth and width, respectively
Cylinder	$\frac{1}{48}$

the channel depth,$\tau_h \sim h^2/D_i$ is short compared to across the channel width $\tau_w \sim w^2/D_i$. Ajdari et al. [20] points out that dispersion in shallow-channels with smooth spanwise height distributions is controlled by the product κPe_w^2, where $Pe_w = wU/D_i$. In wide, shallow channels dispersion, owing to spanwise (width direction) velocity gradients, occurs at rates that are not negligible compared to spanwise diffusion. Statistical sampling of solute molecules along the spanwise direction is, therefore, less efficient and leads to increased dispersion over that of an idealized, infinitely wide channel with the same depth. A key consequence of the analysis is that the largest cross-section dimension controls the time scale to reach the Taylor dispersion limit. For arbitrarily shaped channels, the criteria for achieving Taylor dispersion are then modified to $t_c \gg w^2/D_i$ (where w is the largest cross section scale) and $\sigma \gg a$, where again σ is the characteristic axial dimension of the solute (or interface region) of interest.

38.3.2 Scaling Relations to Estimate Dispersion Effects

In the presence of axial gradients in ionic strength (and conductivity) or pH, both electric field and electroosmotic mobility will vary along the axis of the capillary or microchannel [21]. As discussed earlier, this leads to the generation of internal pressure gradients to satisfy the continuity equation (i.e., mass conservation). In the absence of an external, applied pressure difference, u_p is generated strictly by gradients in EOF mobility $U_{\text{eof}} = \mu_{\text{eof}}(x)E(x)$. For this case, we can estimate the relative importance of Taylor dispersion to molecular diffusion by performing a simple scaling analysis. This exercise highlights the importance of judicious choices of system parameters to minimize dispersion. These choices include separation voltage, EOF suppression strategy, and channel shape and dimensions.

We present an example scaling analysis for dispersion and optimum electric field in a single-interface FASS problem. (The scaling of pressure velocity magnitudes versus local electric field and electroosmotic mobility will also hold for other single-interface preconcentration methods such as the ITP method demonstrated by Jung et al. [22]). This simple case yields approximations as with closed-form analytical expressions. Obtaining estimates for the electroosmotic velocity is the first step. This can be achieved in at least two ways: direct experimental measurement (e.g., in calibration experiments) and theoretical estimates. EOF velocities can be measured under various conditions using the current monitoring method [23], micron-resolution particle image velocimetry measurements [24], or neutral marker tracking [25]. If these measurements are difficult to obtain, EOF velocity can be estimated using various models for the electrical double layer. For thin EDLs, the Helmholtz–Smoluchowski model yields a simple relation [26]:

$$u_{\text{EOF}} = -\frac{\varepsilon \zeta E}{\eta}, \tag{38.17}$$

where ε is the permittivity constant and ζ is the zeta potential [27]. The zeta potential is a function of ionic strength and pH of the electrolyte. Various models and correlations are available in the literature to estimate the zeta potential for various substrates [28–30]. In the presence of axial gradients in conductivity, electric field will also vary along the axis of the channel. Electric field variation can be estimated by invoking conservation of current and Gauss's law. For example, consider the two-zone preconcentration problem in a cylindrical tube as depicted in Figure 38.1. After negligible charge relaxation time scales [13], the following relations hold true [31]:

$$\begin{aligned} &\sigma_{e1}E_1 \cong \sigma_{e2}E_2, \\ &E_1 xL + E_2(1-x)L = V, \end{aligned} \tag{38.18}$$

where σ_e refers to electrical conductivity and x is the fraction of channel filled with σ_{e1}. These equations can be solved simultaneously to obtain E_1 and E_2. Upon deriving the estimates for the

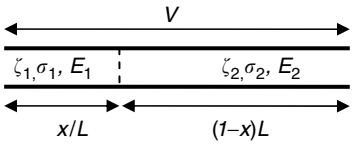

FIGURE 38.1 Schematic representation of a capillary with axial gradient in conductivity, zeta potential, and electric field. The interface is located at distance x/L from the end of the channel (i.e., the applied potential), where x is the fraction of the length L occupied by the liquid 1. The potential drop across the capillary is V.

local electric fields and zeta potentials, the EOF mismatch-induced pressure-driven component of the velocity field can be obtained. To do so, we invoke the continuity equation:

$$U_{\mathrm{EOF},1} + U_{p1} = U_{\mathrm{EOF},2} + U_{p2}, \tag{38.19}$$

where U_{p1} and U_{p2} are related by following:

$$\frac{U_{p1}}{U_{p2}} = -\frac{(1-x)}{x}. \tag{38.20}$$

Finally, the maximum pressure-driven component of the velocity field is (assuming $x < 0.5$):

$$U_{p1} = (U_{\mathrm{EOF},2} - U_{\mathrm{EOF},1})(1-x). \tag{38.21}$$

Burgi and Chien [31] have derived similar relations for estimating internal pressure gradients and for predicting optimum conductivity ratio for FASS. Now, the dispersion coefficient is estimated:

$$D_{\mathrm{eff}} = D + \frac{a^2 U_{p1}^2}{48D} = D + \frac{a^2}{48D}(U_{\mathrm{EOF},2} - U_{\mathrm{EOF},1})^2(1-x)^2. \tag{38.22}$$

Furthermore,

$$U_{\mathrm{EOF},2} - U_{\mathrm{EOF},1} = \varepsilon\frac{(\zeta_1 - \gamma\zeta_2)}{\eta}E_1, \tag{38.23}$$

where $\gamma = \sigma_1/\sigma_2$. Noting $E_1 = E_0/(x + \gamma(1-x))$, where $E_0 = V/L$ is the nominal electric field, we have

$$D_{\mathrm{eff}} = D + \frac{a^2\varepsilon^2 E_0^2}{48D\eta^2}(\zeta_1 - \gamma\zeta_2)\frac{(1-x)^2}{x + \gamma(1-x)}. \tag{38.24}$$

We now assume that we are concerned with a stacking technique such as FASS where variance increases in time. For such a technique, the peak variance due to molecular diffusion and Taylor dispersion scales is

$$\sigma_{\mathrm{total}}^2 \sim 2D_{\mathrm{eff}}\tau_{\mathrm{obs}}. \tag{38.25}$$

Note that D_{eff} varies in space and time as per equation (38.24). However, for scaling purposes the maximum dispersion coefficient can be used. The observation time, τ_{obs}, is a complex quantity to determine, depending on the electrophoretic, electroosmotic, and induced pressure-driven velocities.

A closed form solution may be found in some simple scenarios, but in all cases the time scales linearly with E_0, such that $\tau_{obs} \sim L/\mu_{eff} E_0$, where μ_{eff} is an effective species mobility. Thus,

$$\sigma^2_{total} \sim \left[\frac{a^2\varepsilon^2}{24D\eta^2}(\zeta_1 - \gamma\zeta_2)^2 \frac{(1-x)^2}{x + \gamma(1-x)} \frac{L}{\mu_{eff}}\right] E_0 + \left[2D\frac{L}{\mu_{eff}}\right]\frac{1}{E_0}. \tag{38.26}$$

In this relation, the first term on the right-hand side is the contribution of Taylor dispersion to the overall band broadening. The second is due to molecular diffusion. A key point is that the contribution to the variance due to Taylor dispersion increases with nominal electric field, E_0, whereas variance due to molecular diffusion decreases with electric field, $1/E_0$. This is a consequence of the U_p^2 and therefore, E_0^2 scaling of D_{eff} on the one hand, and the L/u and therefore, $1/E_0$ scaling of time. Therefore, there exists an optimum electric field that will minimize the peak broadening. This optimum electric field can be derived by minimizing the variance with respect to field to obtain

$$E_{optimum} \sim \sqrt{\frac{48D^2\eta^2(x + \gamma(1-x))}{a^2\varepsilon^2(\zeta_1 - \gamma\zeta_2)^2(1-x)^2}}. \tag{38.27}$$

As we discuss later in this chapter, techniques achieving a steady-state dispersion-limited width typically also have optimum electric fields that reduce dispersion. At negligible Taylor dispersion conditions (i.e., low electric fields), the sample axial dimension is determined by a balance between electrophoretic focusing fluxes and molecular diffusion. Plug axial dimension, therefore, scales as D/E_0 (see Equations 38.40, 38.41, 38.44, and associated discussions). At higher electric fields, Taylor dispersion becomes important and axial dimensions scale as D_{eff}/E_0. At sufficiently high fields, the Taylor dispersion term, which scales as $a^2\varepsilon^2E_0^2/(48D\eta^2)$, dominates and then interface width again scales as E_0.

In all cases, the optimum field for minimization of Taylor dispersion is a function of sample (through D), channel geometry, solution viscosity, and zeta potential value for a given conductivity ratio and solution permittivity. Finally, we note the earlier analysis neglects the effects of Joule heating [32,33] on dispersion. Joule heating places additional constraints on the optimum field as temperature rise is a function of both conductivity distribution and pore diameter. We, however, stress the main purpose of the analysis is to argue that all preconcentration phenomena have optimum fields and that they are often limited by the dispersion associated with even residual EOF.

38.4 PRACTICAL APPLICATIONS

38.4.1 Field-Amplified Sample Stacking

38.4.1.1 Introduction

Field-amplified sample stacking is a fairly widely applicable method of achieving increased sensitivity for capillary and on-chip assays in a scheme that is easily integrated with electrophoretic separation techniques [4,34–43]. FASS is typically used as a preconcentration step that occurs before the electrophoretic separation of analyte ions.

The transport phenomena associated with FASS (as in all preconcentration methods) are, in general, a complex coupling of convective–diffusion, electrostatics, and electrokinetics along with the unsteady effects associated with the response of the electrical double layer to varying bulk ion concentrations. The detailed understanding of the process dynamics is important for optimization of high-sensitivity systems. The effects of EOF on preconcentration and separation are very important to studies of FASS as even slight EOF couples with axial conductivity gradients to generate internal

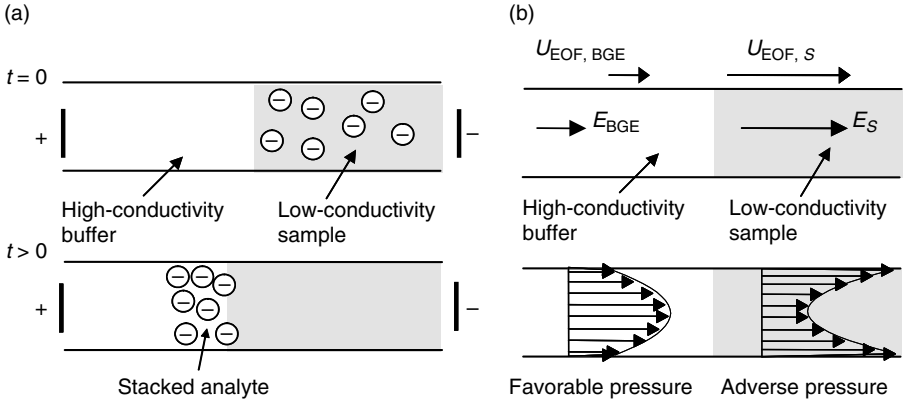

FIGURE 38.2 (a) Schematic diagram showing FASS of anionic species in the absence of EOF. A gradient in the BGE ion concentration is established. The sample is in a region of locally low conductivity. Upon application of an electric field, the axial gradient in conductivity results in an electric field gradient. Since area-averaged current density is uniform along the axis of the channel, the low conductivity section is a region of high electric field, and the region of high conductivity contains relatively low electric field. As sample ions exit the high field/high electrophoretic velocity region and enter the low velocity region, they locally accumulate and increase in concentration. (b) Stacking in the presence of EOF. Gradients in conductivity generate axial variation in electric field and electroosmotic mobility. The system generates internal pressure gradients, which tend to disperse the sample.

pressure gradients. These internal pressure gradients disperse the sample and thereby, limit the practically achievable concentration enhancement.

38.4.1.2 Basic Theory and Implementation

The principle behind FASS is shown schematically in Figure 38.2a. An axial gradient in ionic conductivity (and therefore electric field) is achieved by preparing the sample in an electrolyte solution of lower concentration than the BGE. Upon application of an axial potential gradient, the sample region acts as a high electrical resistance zone in series with the rest of the channel and a locally high electric field is generated within the sample zone. Under the influence of electric field, sample ions migrate from the high to low drift velocity region. This leads to a local accumulation or "stacking" of sample ions near the interface between high and low conductivity regions. This stacking increases sample concentration and results in an increased signal. The process depicted in Figure 38.2a is for an idealized case where diffusion and advection are neglected. The maximum concentration enhancement is given by a conservation of species at the interface

$$\frac{C_{\text{Stacked}}}{C_{\text{Initial}}} = \frac{E_S}{E_{\text{BGE}}} = \gamma, \tag{38.28}$$

where E_S and E_{BGE} are the electric field in the sample and the BGE regions, respectively. In essence, FASS relies strictly on electric field gradients generated by spatial variations in ion density. This makes FASS unlike other preconcentration techniques (such as ITP and IEF), which require more specific buffer chemistries and ion mobilities. For example, FASS can be implemented with the same type of ions in the BGE and sample zones. As such, FASS provides flexibility in the choice of BGE buffer chemistry and can nearly always be performed under well-controlled pH conditions.

Figure 38.2b shows a more realistic system where finite EOF is present. The gradient in the electrolyte concentration required for stacking leads to a gradient in electric field and electroosmotic mobility. This causes a mismatch of electroosmotic velocity and hence generation of a pressure

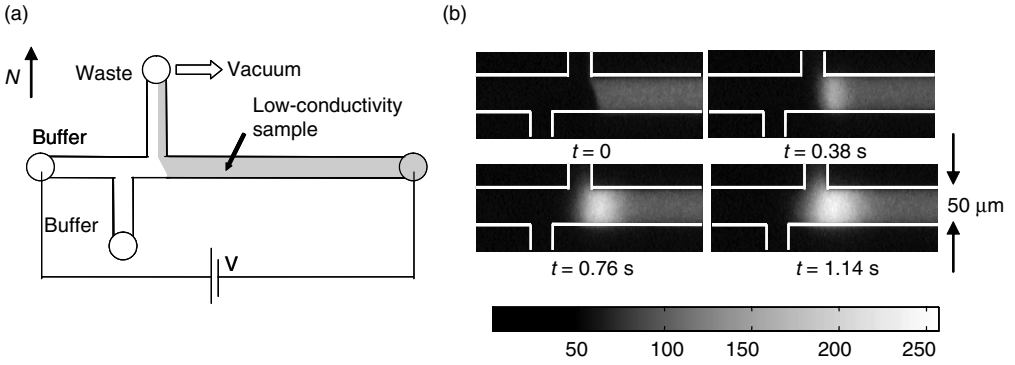

FIGURE 38.3 Single interface stacking experiments. (a) Schematic diagram of a microchip. Width and centerline depth of channels were 50 μm and 20 μm, respectively. (b) Epifluorescence CCD images showing establishment of initial condition for conductivity gradient and subsequent stacking across interface. The sample was anionic 17 μm bodipy dye and the buffer was HEPES at pH = 7.

gradient (consistent with the continuity constraint). The pressure gradient tends to disperse the concentration fields and thereby lower the efficiency of stacking.

FASS has been applied in a variety of assay formats in both capillaries and microchips. The configurations can be broadly classified as (1) single interface configuration and (2) finite-plug configuration. The single interface configuration includes techniques such as field-amplified sample injection (FASI) [36,37,44], large volume sample stacking (LVSS) [38], and Head-Column FASS [45]. These techniques involve a single interface between the sample region and BGE. In these techniques, the volume of sample loaded into the capillary or the microchannel often exceeds the total volume of (initially low concentration) sample loaded into the capillary, or the microchannel can exceed the total volume of the capillary. In contrast, the finite-plug technique involves sample zones of fixed size. The sample zone size can be defined by duration of sample injection by either electrokinetic flows or by hydrodynamics flow. In microchannel networks, the sample size can be accurately controlled by chip geometry, for example, by using pinched-injection or staggered-T injection [46–48].

Figure 38.3 shows schematic representation of microchip-based single-interface FASS system. The interface between high and low conductivity buffer regions is generated by applying a vacuum at the north reservoir. Once a buffer–buffer interface is established, the vacuum is released and an axial electric field is applied. Upon application of an axial electric field along the west-to-east direction, sample stacks at the interface between buffer streams. Figure 38.3b shows images of the stacking process at selected times. In Figure 38.4, instantaneous images of stacking process are shown for a case where EOF was not suppressed. Since the EOF velocity in all regions is greater than the negative electrophoretic velocity of fluorescein dye, the stacked region moves in the direction of EOF. The images clearly show the favorable pressure-gradient-induced curvature of the stacked ions on the downstream (left-hand) side of the interface. As described earlier, these pressure gradients act to disperse sample and reduce the efficiency of FASS. From Figures 38.3b and 38.4, the efficacy of the EOF-suppression method is apparent as the conductivity interface is nearly stationary and there is negligible pressure-induced curvature of stacked analyte. Figure 38.5 shows the temporal development of the spatial concentration distribution of sample ions. The peak intensity increases roughly exponentially at first and then saturates at a maximum achievable concentration enhancement of γ.

38.4.1.3 Dispersion Theory

In most electrophoretic experiments, the quantity of practical interest is the cross-sectional area-averaged concentration distribution of sample ions. This quantity is, for example, proportional to the

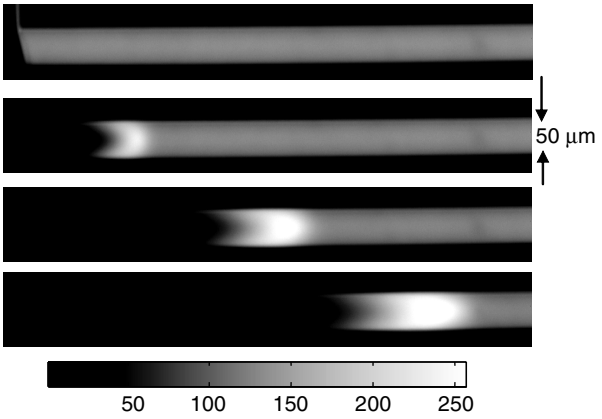

FIGURE 38.4 CCD images of on-chip FASS in an untreated channel with significant EOF mobility. The images clearly show the development of stacked fluorescein in the favorable pressure gradient region (i.e., the high conductivity region). The sample was 25 μm fluorescein dye dissolved in 5 mM Borate buffer. The BGE for this particular experiment was 25 mM Borate buffer (pH = 9.2). The electric field in the sample region was 50 V/cm and $\gamma = 4$.

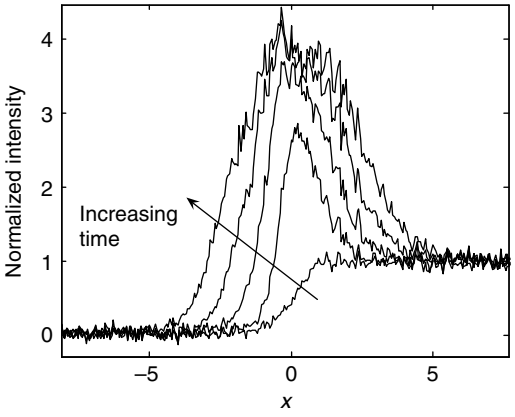

FIGURE 38.5 Measured axial intensity profiles for sample ions. The profiles were obtained by averaging two-dimensional image intensity data along the width of the channel. The applied nominal electric field was 588 V/cm and $\gamma = 4$. Time between individual profiles was 0.15 s.

measured signal intensity of line-of-sight optical integrators such as pointwise fluorescence detectors, transmitted-mode absorption detectors, and width-averaged electrophoregrams from charge-coupled device (CCD) arrays. This signal determines the key detectability constraints of electrophoretic separations [3]. As described earlier, Taylor dispersion analysis allows us to develop cross-sectional area-averaged transport equations. Such models provide useful insight into the physics of the process and lead to the identification of key parameters that can be used to develop optimization strategies for FASS experiments.

The FASS model requires description of electromigration, diffusion, and advection of sample ions as well as BGE ions. The general system of equations is highly coupled and nonlinear and, therefore, difficult to solve. However, the concentration of sample ions is much smaller than the buffer ions (typically μM sample ions concentration or less versus order 1 mM buffer ion concentrations). Therefore, we can decouple the buffer and sample ion concentration fields. Using this approach, Bharadwaj and Santiago [4] have developed a dynamic model for FASS in a flat-plate

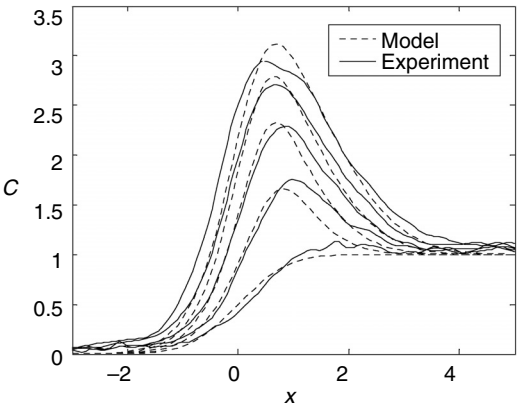

FIGURE 38.6 Comparison of model prections and measured concentration profiles. $\gamma = 4$, $E_0 = 379$ V/cm, and time-between-frames was 76 ms. The model parameters are $Pe_e = 55$, $\alpha = 0.23$, $\beta = 0.28$, $\delta = 1.27$.

geometry. The analysis provides the following equation for the cross-sectional area-averaged sample ion distribution, C_S:

$$\frac{\partial C_S}{\partial t} + \alpha\langle u\rangle \frac{\partial C_S}{\partial x} = D\frac{\partial^2 C_S}{\partial x^2}\frac{1}{Pe_e} + \alpha^2\beta^2 Pe_e \frac{8g(x,t)}{105D}\frac{\partial}{\partial x}\left(g(x,t)\frac{\partial C_S}{\partial x}\right) - z_S\mu_S\frac{\partial (C_S E)}{\partial x}. \quad (38.29)$$

The parameters governing this system of equations are

$$Pe_e = \frac{E_0\mu_{\text{eph}}Fs_S}{D_S}; \quad \alpha = \frac{-\varepsilon_0\varepsilon_r\zeta/\eta}{\mu_{\text{eph}}} = \frac{\mu_{\text{eof}}}{\mu_{\text{eph}}}; \quad \beta = \frac{d}{s_S}; \quad \text{and} \quad \delta = \frac{s_B}{s_S}.$$

Pe_e is the electric Peclet number, expressed as the ratio of diffusion time to electromigration time; α is the ratio of electroosmosis to electrophoretic mobility; β is the ratio of channel width to characteristic length scale for the initial sample ion concentration distribution; and δ is the ratio of the length scale of the initial BGE and sample ion concentration gradients. Here, d is the channel depth, s_S and s_B are the initial sample and BGE ion concentration gradients, and E_0 is the nominal electric field. The function $g(x,t)$ in the advective dispersion term accounts for the axial variation in pressure-driven velocity profile (cf. Figure 38.2).

Figure 38.6 shows comparisons between dispersion model predictions and experimentally measured concentration profiles. Experiments are shown for $\gamma = 4$ and 9 and E_S values of 379 and 588 V/cm. There is a quantitative agreement between measured area-averaged concentration profiles and the model prediction throughout the time of observation. The model predictions were obtained by solving Equation 38.29. As shown in Figure 38.3b, for times approaching 1 s, the region of high area-averaged concentration becomes two-dimensional as it enters the staggered-T injection region of the system, which cannot be captured by one-dimensional model. The dispersion model is able to capture important features such as the development of peak width and the temporal growth of the maximum concentration. Also, the model describes convective–electromigration–diffusion dynamics in a purely two-dimensional flow in a wide, shallow channel (neglecting the influence of side walls). In reality, however, the microchannels in the experiment have a D-shape characteristic of an isotropic etch with a width to maximum depth ratio of 2.5. This assumption may be improved in future refinements of the dispersion model. For example, Dutta and Leighton [6] have investigated the effect of isotropic-etched microchannel geometries on the dispersion coefficient for simple pressure-driven flows. Their analysis shows, in the Taylor dispersion limit (ruled by the widest channel dimension), the dispersion coefficients for the D-shaped channels can be three to four times

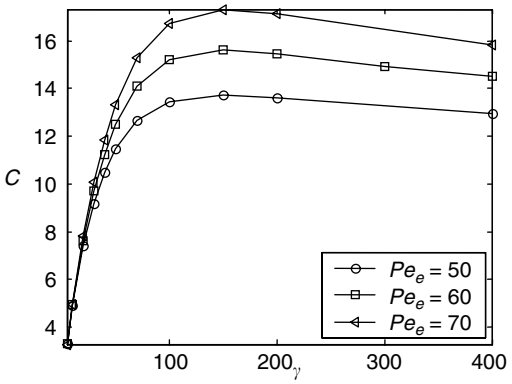

FIGURE 38.7 Optimum value of γ for fixed stacking times of 1 s. The parameters for the dispersion model are: $\alpha = 0.5$, $\beta = 2$, and $\delta = 1$. For a given analysis time and fixed values of Pe_e, α, β, and δ, there is a unique value of γ that provides maximum concentration enhancement.

larger than those predicted by simple two-dimensional analysis. Such advective–diffusion effects would be most important in flow for large γ values (associated with larger internally generated pressure gradients) and the large Peclet numbers associated with high electric fields. Another possible refinement of the model would include dispersive effects due to Joule heating [49], which should also lead to reduction in the rate of concentration increase.

38.4.1.4 Performance and Guidelines

In this section, we summarize some parametric and optimization results from dispersion models. First, we consider the effect of conductivity ratio, γ, on stacking efficiency. Figure 38.7 shows clearly that there is an optimum value of γ for a given set of parameters and analysis time. In these plots, the analysis time is fixed as we are interested in FASS as a preconcentration step before electrophoretic separation. These fixed-time comparisons help to determine the time needed to achieve adequate concentration enhancement and the initial condition of the subsequent uniform-conductivity separation process. These model predictions were generated with a parametric variation study using the numerical model described earlier. This result is in contrast with the ideal concentration factor described earlier, which shows that increasing γ always increases the concentration enhancement (Equation 38.28). This in an important feature of the dispersion analysis as it gives experimentalists a method of choosing values of γ to yield optimal signal detections.

The existence of an optimal value of γ can be better understood by considering the scaling of the parameters of interest. Equation 38.28 shows that the maximum sample concentration is proportional to γ:

$$C_{C,\max} \propto \gamma. \tag{38.30}$$

In contrast, the ratio of the EOF velocities in the low-conductivity region to the value in the high-conductivity region scales is

$$\frac{U_{\mathrm{EOF},S}}{U_{\mathrm{EOF},B}} \sim \frac{\zeta_S E_S}{\zeta_B E_B} \sim \gamma^{1+n}. \tag{38.31}$$

The parameter n refers to the ratio of the zeta potential in the sample and the BGE regions. Typical values of this parameter range between 0.2 and 0.3 [50,51], so that the advective dispersion effects of mismatched slip velocities is negligible for low γ but dominates at high γ. An analogous scaling

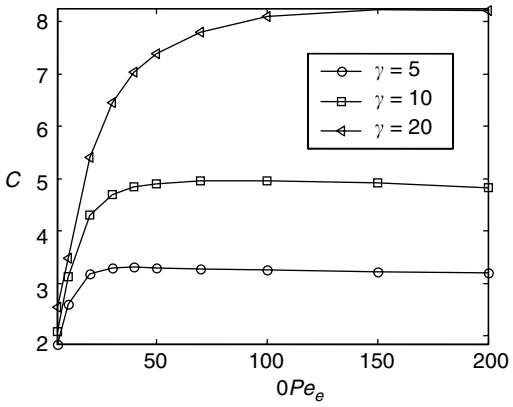

FIGURE 38.8 Optimum value of Pe_e for a fixed stacking time of 1 s. The parameters for the dispersion model are $\alpha = 0.5$, $\beta = 2$, and $\delta = 1$. At low Pe_e, diffusive dispersion dominates and concentration enhancement suffers. At high Pe_e, advective dispersion is dominant and again concentration enhancement suffers. For fixed γ and analysis time, there is a unique, optimal Pe_e (e.g., an optimal electric field for a given channel system) which results in maximum concentration increase.

observation was made by Burgi and Chien [31]. They discuss the existence of an optimum γ using simple scaling arguments. They developed an algebraic model for the long-time behavior of a finite-length sample plug variance as a function of γ, using a one-dimensional Taylor dispersion approximation. In contrast to their model, the dynamic model described here allows quantitative prediction of both temporal and spatial development of the sample ion, BGE ions, and electric field profiles.

Another important parameter determining the convective dispersion and hence, rate of concentration increase in FASS is α, or the ratio of electroosmotic and electrophoretic mobilities. For a typical value of electrophoretic mobility (e.g., 3E−8 $m^2\ V^{-1}\ s^{-1}$), α is approximately equal to 2 for glass microchips. Therefore, the dispersion dynamics of untreated glass chips are well in the advection regime. However, at least an order of magnitude reduction in electroosmotic mobility is possible by dynamic surface coatings using neutral water-soluble polymers [52]. It is, therefore, interesting to experimentalist to quantify the importance of suppressing EOF in determining maximum achievable concentration increases. Bharadwaj and Santiago [4] show that, even for the case of a 10-fold decrease in electroosmotic mobility ($\alpha = 0.2$), there is significant convective dispersion. The preconcentration time required to reach the maximum concentration enhancement can be as much as 50% longer for $\alpha = 0.2$ case as compared to a case where there is no EOF. This result has important consequences in the design of microchip-based FASS systems because a slower rate of concentration increase can adversely affect both the amount of sample required per separation and the throughput of the device. To increase the rate of concentration enhancement, the electric field and Peclet number should be increased.

Figure 38.8 describes the effect of Peclet number, $Pe_e = E_0 \mu_{\text{eph}} F s_S / D_S$, on maximum concentration achievable for a given analysis time. Initially, increases in Pe_e are favorable for concentration enhancement. This is due to a reduced contribution of molecular diffusion, which scales as Pe_e^{-1}. However, as Pe_e is increased further, the concentration increase slows down and, past a critical Pe_e, the achievable concentration begins to decrease. The latter effect is due to the aforementioned fact that convective dispersion increases with increasing Pe_e. Equation 38.29 shows the dispersion term scales as $\alpha^2 \beta^2 Pe_e$. There is, therefore, an optimum value of Pe_e (e.g., an optimum electric field for a given process and geometry) for a given analysis time and fixed values of γ, α, and β. Note that the optimum value of Pe_e may be somewhat smaller in practice than that predicted by our dispersion model since we do not account for the effects of Joule heating [49]. Joule heating is proportional to the square of local electric field and is expected to be important for very high field strengths and relatively large channels.

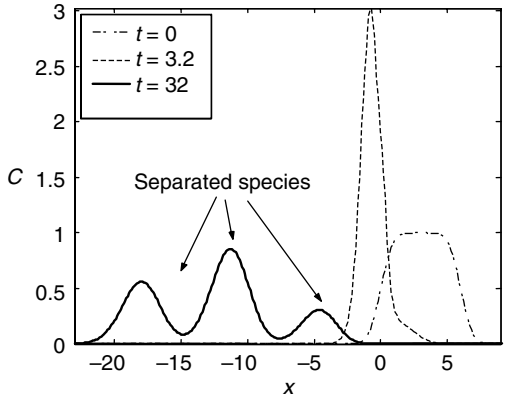

FIGURE 38.9 Stacking and separation dynamics of three negatively charged sample species. The model parameters are $Pe_e = 40$, $\gamma = 5$, $\beta = 2$, $\alpha = 0.05$, $\delta = 1$, and $h = 6$. The dimensionless electrophoretic mobilities of the species are 1, 2, and 3, respectively. The initial dimensionless concentrations of the sample species are 1/6, 1/2, and 1/3, respectively.

Finally, Figure 38.9 shows model results for sample stacking and separation dynamics of a finite injection volume (initially approximately six channel depths wide) of three anionic sample ions. Initially, there is rapid stacking (accumulation) of the sample ions as they exit the low conductivity region and enter the high conductivity region. Once sample ions enter the high conductivity region, sample stacking ends and ions are subsequently electrophoretically separated into three distinct peaks. The dispersion model can be used to optimally design FASS-based electrophoretic separation systems for the analysis of multiple sample species. For example, the model predictions can guide the location of detector and width of initial sample plug to ensure adequate signal-to-noise ratio (SNR) and resolution.

38.4.2 Temperature Gradient Focusing

38.4.2.1 Introduction

So far, we have alluded to a number of preconcentration techniques that are of interest to the CE community and, in the previous section, we examined FASS in detail. In this section, we consider dispersion as it relates to focusing techniques. The quintessential focusing technique is IEF [53–55]. In IEF, charged species migrate through a pH gradient under the influence of an electric field until they reach their isoelectric, or pI, point. At the pI, a species becomes net neutral and ceases to migrate. While this is the most common focusing technique, it is not the most general from the perspective of dispersion analysis and scaling. Consequently, we choose microfluidic temperature gradient focusing (TGF) as it represents an excellent case study in dispersion and provides a more general model. The approach and discussions presented can be extended to the analysis of Taylor dispersion in IEF.

TGF is a form of electric field gradient focusing, where a temperature-induced gradient in electric field helps produce the gradient in electrophoretic velocity required for focusing (in contrast to IEF, where the focusing effect is caused by the changing charge on an ampholyte). TGF was first described in a seminal paper by Ross and Locascio [56], where they demonstrated the successful focusing of charged fluorescent dyes, amino acids, green fluorescent protein, DNA, and polystyrene particles, illustrating the general utility of TGF. TGF has subsequently been extended to DNA hybridization assays and single nucleotide polymorphism detection [57], as well as the detection of chiral enantiomers [58]. Focusing of neutral and ionic hydrophobic analytes (e.g., coumarin)

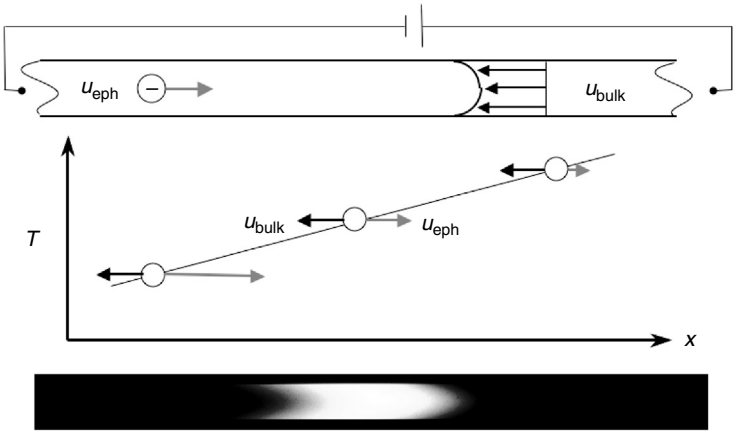

FIGURE 38.10 Schematic of TGF process with advective dispersion. An electrophoretic velocity is countered by an opposing liquid flow, composed of both pressure-driven and electroosmototic flow (top). A temperature gradient is applied to a microchannel, inducing a gradient in the electrophoretic velocity of an analyte. The analyte focuses where the electrophoretic and convective ("bulk") fluxes sum to zero (middle). Both molecular diffusion and advective dispersion broaden the band about the focus point. The bottom image shows Bodipy focused in a 20 by 200 μm wide channel with an applied electric field and temperature gradient of 60 V/mm and 10°C/mm, respectively.

has also been achieved [59,60] using TGF combined with micellar electrokinetic chromatography (MEKC). The capabilities of TGF allow it to be used in analytical (i.e., detection and separation) and preparative (i.e., concentration and purification) applications. In both applications, minimization of dispersion is an important design goal.

We have already discussed the basics of dispersion, noting how decreased dispersion improves resolution and sensitivity in separation applications [61], and also yields improved dynamics for concentration and purification applications [4]. However, there are some key differences to consider when comparing focusing techniques such as TGF with other techniques. We describe the basics of TGF theory, implementation details, and the modifications to Taylor dispersion required for TGF. Finally, we present tips for empirical optimization of TGF preconcentration factors and resolution.

38.4.2.2 Basic Theory and Implementation

Temperature gradient focusing focuses charged species by balancing an axially varying electrophoretic flux with a counterflow, causing species to focus at locations where their net fluxes sum to zero (Figure 38.10) [56].

$$\langle u_{\text{bulk}} \rangle + u_{\text{eph}}(x_{\text{foc}}) = 0, \tag{38.32}$$

where x_{foc} is the focus location for the species in question and "bulk" refers to the net effect of both pressure-driven flow and electroosmosis. Note that, unlike IEF, the electrophoretic velocity of the charged species is always nonzero, so a counterflow, and its associated dispersive effects, is always present and significant. In practice, the counterflow is provided by a combination of flow due to electroosmosis and flow caused by an externally applied pressure difference. Variation in electrophoretic flux is accomplished by applying a temperature gradient along the axis of the microchannel and by using a buffer with a temperature-dependent ionic strength (e.g., due to temperature-dependent dissociation of a weak electrolyte).

Within the channel, local electric field is inversely proportional to conductivity, which in turn is a function of local viscosity and ion density. Using the convention of Ross et al. [56], we write the conductivity as $\sigma(T) = \mu_0\sigma_0/(\mu f)$, where μ_0 and σ_0 are the buffer viscosity and conductivity at a defined reference temperature, $\mu(T)$ is the viscosity, and $f(T)$ is a nondimensional function incorporating any remaining conductivity dependencies (primarily the change in ionic strength). A similar decomposition is applied to the electrophoretic mobility, yielding $v_{\text{eph}} = v_{0,\text{eph}}\mu_0/(\mu f_{\text{eph}})$, where $v_{0,\text{eph}}$ is the analyte's electrophoretic mobility at the reference temperature, and $f_{\text{eph}}(T)$ accounts for any other temperature dependencies. The usefulness of this decomposition becomes apparent when we assume uniform current, I, use Ohm's law to determine the local electric field, and solve for the electrophoretic velocity:

$$u_{\text{eph}} = v_{0,\text{eph}} E_0 f / f_{\text{eph}}, \tag{38.33}$$

where $E_0 = I/A\sigma_0$ and A is the channel cross-sectional area. Most analyses assume $f_{\text{eph}}(T)$ remains near unity, which is equivalent to assuming that the ion has a charge and drag coefficient independent of temperature. In this case, we see the electrophoretic velocity is a function only of the temperature, through f. In addition, we note the rate of (global) mass accumulation in the entire volume of a channel due to electrophoretic focusing is proportional to the difference in f on the boundaries. However, for a differential volume or for linear $f(T(x))$, the focusing is proportional to the gradient of f.

TGF has been implemented in a variety of microfluidic formats, including channels imprinted in polymer substrates and embedded capillaries [56,62]. In most cases, the temperature gradient is imposed by mounting the channel across temperature-regulated blocks, such that the temperature gradient is established via thermal conduction in the gap between the blocks. Figure 38.11 shows

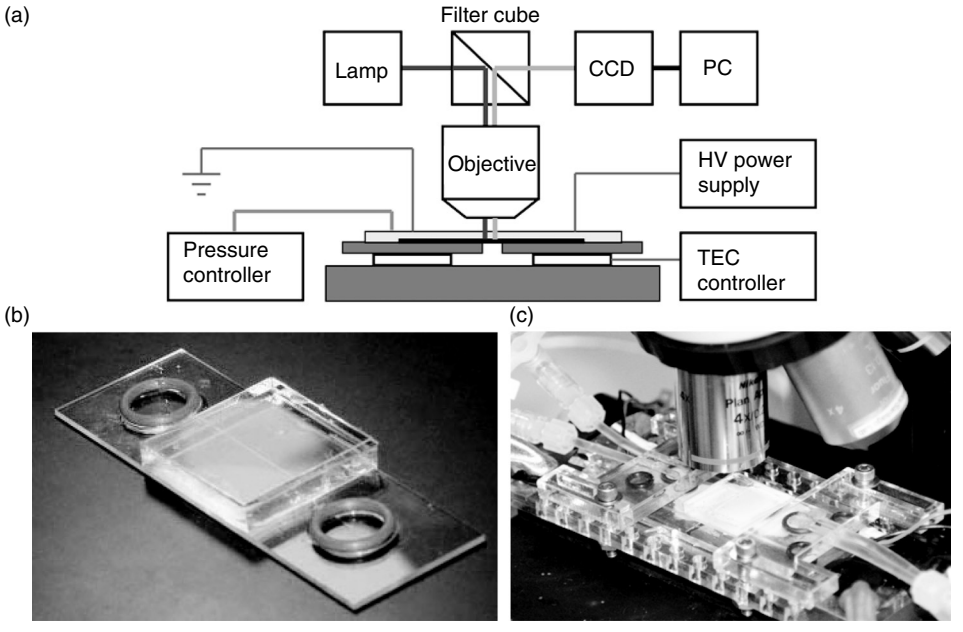

FIGURE 38.11 Control schematic and images of TGF fixture and capillary assembly. The TGF assembly (a) provides the thermal, fluidic, and electrical interface to the microchannel. A temperature gradient is established across a gap between two copper plates, each heated or cooled by a thermoelectric (Peltier) device. Pressure control is accomplished by adjusting the relative heights of two external reservoirs. The capillary assembly (b) consists of a 20 by 200 μm rectangular glass borosilicate capillary that spans the distance between two O-ring reservoirs and underneath an insulating PDMS block. In the assembly photo (c), the capillary assembly is mounted on the TGF fixture. The encapsulating PDMS block is located directly below the objective, and the fluidic manifolds are to the left and right of the block [62].

one such implementation. Alternatively, Joule heating has also been used to form the temperature gradient independent of external fixtures [56,63].

38.4.2.3 Dispersion Theory

To analyze dispersion in TGF, we must modify our previous derivation to account for changes due to the temperature gradient. This includes an axially varying electrophoretic velocity and diffusivity. In its most general form, the transport equation becomes

$$\frac{\partial c}{\partial t} + \mathbf{u}_{\text{bulk}} \cdot \nabla c + \nabla \cdot \left(\mathbf{u}_{\text{eph}} c\right) = \nabla \cdot \nabla \left(Dc\right), \tag{38.34}$$

where c is the concentration of the sample analyte and D is the analyte's molecular diffusivity. Note the placement of the electrophoretic velocity and diffusivity within the gradient operators. In particular, the placement of the diffusivity within the second gradient operator reflects the use of the Fokker–Planck diffusivity law, $\mathbf{J} = -\nabla(Dc)$. Although it is common practice to use Fick's law for the diffusive flux (yielding the traditional $\nabla \cdot D\nabla c$), Fick's law strictly applies only to diffusion with homogeneous D [64]. To recover the more familiar diffusion representation, we differentiate, yielding the terms, $D\nabla c$ and $c\nabla D$. The latter term thus represents a flux due to a diffusivity-induced velocity, ∇D, which is typically small in comparison to the electrophoretic velocity.

For a purely axial temperature gradient, if the cross section mean decomposition is again performed, a new mean concentration transport equation is derived

$$\frac{\partial \langle c \rangle}{\partial t} + \langle u_{\text{bulk}} \rangle \frac{\partial \langle c \rangle}{\partial x} = \frac{\partial}{\partial x}(\langle u_{\text{eph}} \rangle \langle c \rangle) = \frac{\partial}{\partial x}\left(D\frac{\partial \langle c \rangle}{\partial x} - \langle u'_{\text{bulk}} c' \rangle\right). \tag{38.35}$$

The deviation transport equation again reduces to a form analogous to Equation 38.11 following our scaling arguments, although with one exception, the characteristic time scale for TGF is no longer the observation time, but is instead the focusing time for a nondiffusive particle approaching its focal point, τ_{foc}. (See solution for form of τ_{foc}.) Note that if any of these assumptions are violated, then new dispersion mechanisms arise. For example, if τ_{foc} is of order a^2/D or less, then ballistic dispersion [20] can become significant. The correlation term on the right-hand side of Equation 38.35 once again corresponds to the advective dispersion arising from transverse variations in the axial velocity. To evaluate this term, we need an expression for u'.

An analytical solution for u' was derived by Huber and Santiago [62]. Using a decomposition on the Helmholtz–Smolukowski equation similar to that performed by Ross for the electrophoretic velocity, they determined the nonuniform electroosmotic slip velocity to be

$$u_{eo} = v_{eo,0} E_0 f(T) g(T), \tag{38.36}$$

where v_{eo} is the electroosmotic mobility, $g(T) \equiv v_{eo}(T)\mu(T)/v_{eo,0}\mu_0 = \varepsilon(T)\zeta(T)/\varepsilon_0\zeta_0$, ε is the permittivity, ζ is the zeta potential, and the subscript zero indicates a value at the reference temperature [16]. By extending the lubrication flow solution of Ghosal [65] to include variable viscosity and the nonuniform electroosmotic slip velocity of Equation 38.3, Huber and Santiago derived an analytical expression for the bulk velocity, from which the deviation velocity was determined:

$$u'_{\text{bulk}} = U_p \left(\frac{1}{2} - \frac{3y^2}{2a^2}\right), \tag{38.37}$$

$$U_p = \frac{a^2}{3\{\mu\}} \frac{\Delta P}{L_{\text{ch}}} + v_{eo,0} E_0 \frac{\{\mu f g\}}{\{\mu\}} - v_{eo,0} E_0 f g, \tag{38.38}$$

where a is the channel half-height, L_{ch} is the length of the channel, ΔP the applied pressure difference, and the curved brackets indicate an axial mean over the length of the channel. We see the flow field is a superposition of a uniform electroosmotic component and a parabolic (in y) pressure-driven component (for flow between parallel plates). The two are linked through continuity, so as one decreases, the other must increase. Thus, U_p, the pressure-driven flow component, contains both the externally applied pressure gradient and the internally generated pressure gradient, which results from the local slip velocity deviating from the axial average. Note that the axially averaged terms are uniform and constant, and f and g are functions of T; therefore, the velocity profile varies in x in response to axial temperature changes.

We analyze a flat-plate geometry again for simplicity and as an approximation to the full focusing problem. This implies, we are interested in characteristic focusing times much longer than that for molecular diffusion along the depth but not for spanwise diffusion along the width of the channel. This implies that our analysis is an estimate of the maximum concentrations achieved over these relatively short focusing times (along the centerline of the channel) and does not account for the finite amount of dispersion introduced by spanwise velocity gradients. Improvements on this model are discussed in the following text.

Given u' and c', the advective dispersion term may be determined, which yields

$$\frac{\partial \langle c \rangle}{\partial t} + \langle u_{\text{bulk}} \rangle \cdot \frac{\partial \langle c \rangle}{\partial x} + \frac{\partial}{\partial x}(\langle u_{\text{eph}} \rangle \langle c \rangle) = \frac{\partial}{\partial x}\left(D_{\text{eff}} \frac{\partial \langle c \rangle}{\partial x} \right), \tag{38.39}$$

$$D_{\text{eff}} = D\left(1 + \frac{2}{105}\frac{U_p^2 a^2}{D^2}\right). \tag{38.40}$$

This 1-D convection–diffusion equation has features of the Taylor–Aris dispersion equation. However, in contrast to Taylor–Aris, here D_{eff} is a function of temperature and the axial coordinate, as it depends on both D and U_p. When f is a linear function of the axial dimension, Equation 38.39 can be solved in closed form subject to the form of D_{eff}. If D_{eff} is uniform, the solution is a Gaussian with peak variance $\sigma^2 = 2D_{\text{eff}}\tau_{\text{foc}}$, where $\tau_{\text{foc}} = 1/2E_0 v_0 |\mathrm{d}f/\mathrm{d}x|$. If D_{eff} is also a linear function of x, the solution is

$$c = c_0 \exp\left\{ -\frac{x/L - \ln(1 + x/L)}{\sigma^2/L^2} \right\}, \tag{38.41}$$

where c_0 is the peak height and $L = D_{\text{eff}}(0)/(\mathrm{d}D_{\text{eff}}/\mathrm{d}x)$ [62]. Although unusual in form, this solution produces Gaussian-like peaks with a skew that grows with the slope of D_{eff}. For more general cases, the equation can be solved numerically.

Figure 38.12 shows sample full-field fluorescence images of focused Bodipy proprionic acid in an applied temperature gradient of 10°C/mm and electric fields from 1 to 215 V/mm. The two cases illustrate different dispersion regimes. The images on the left show focusing in the molecular diffusion dominated regime. Note the lack of spanwise curvature in the peaks and the near inverse square root dependence of peak width on electric field (dotted line). The images on the right-hand side show focusing experiments where the Taylor dispersion criteria are violated about $E_0 = 40$ V/mm and there is enhanced advective (or ballistic) dispersion [20]. The solid line is a theoretical prediction for the peak width based on an heuristic ballistic dispersion model [66]. In both cases the direction of electrophoretic flux is left to right, while the bulk flow is right to left, driven by electroosmosis. The experimental and theoretical peak widths agree closely with some deviation at low fields, where the focused peak remains slightly "over-focused" as field was decreased, having had insufficient time to diffuse out to full width.

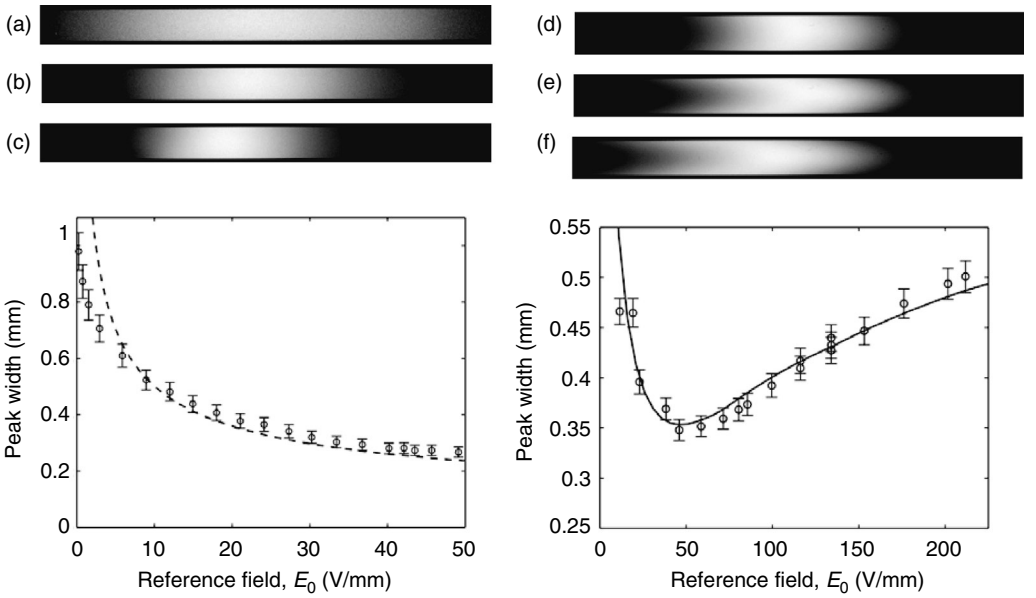

FIGURE 38.12 Bodipy peak images and width as function of reference field. The images show focused Bodipy dye within a 20 × 200 μm rectangular capillary, while the bottom figures plot the peak widths versus electric field as determined by the fitting of Gaussian profiles to each peak. The applied temperature gradient was 10°C/mm and the applied electric fields ranged from 1 to 215 V/mm. The left hand side shows results for focusing in the molecular diffusion dominated regime. The current-normalized fields, E_0, were (a) −1.5, (b) −15, and (c) −30 V/mm. The right hand gives results which violate the Taylor scaling arguments above 40 V/mm and thus feature enhanced ballistic dispersion. (Note the curvature in the images of the peaks.) The fields were (d) −38, (e) −81, and (f) −212 V/mm [62,66].

38.4.2.4 Performance and Guidelines

As we have described, TGF has successfully demonstrated the simultaneous concentration and separation of a wide range of species in a variety of implementations. Key figures of merit for TGF as a separation modality are the concentration factor and peak capacity. Static TGF, where the externally applied pressure remains constant, has demonstrated concentration factors in excess of 20,000 but is limited to peak capacities <10 [56]. As a result, there has been recent work to develop a dynamic form of TGF called scanning TGF [67], where the externally applied pressure is varied with time. This technique allows higher peak capacity and tunable resolution and concentration by adjusting the rate at which the procedure scans through the applied pressures.

In implementation, the complexities of TGF extend beyond that due to advective dispersion and encompass system design details such as device geometry, temperature control, and buffer selection. In static TGF, larger temperature gradients produce faster focusing and sharper peaks but reduce resolution [56]. The latter may be addressable using scanning TGF, but particular attention must be paid to the temperatures within the system because analytes of interest (e.g., enzymes) may be extremely sensitive to temperature and Joule heating may adversely influence the temperature gradients. In order to produce desired temperature profiles, designers must consider conductive and convective heat transfer within the channel, Joule heating due to the electric field, and heat transfer from the channel to its fixture and the environment. While it is possible to model these effects, in most cases, empirical studies will be required to validate models and refine optimizations.

Optimization of TGF preconcentration and (static) resolution is similar to other sample preconcentration methods. As described earlier, the contribution of molecular diffusion to the total peak variance scales as $1/E$, while the Taylor dispersion coefficient scales as U_p^2 and therefore, E^2. Sample

peak variance, therefore, scales as $1/E$ at low fields and as E at high fields. Thus, there will (again) be an optimal field strength that minimizes the overall peak width. Finally, we note that reducing the characteristic width of the channel simultaneously decreases the amount of Taylor dispersion and Joule heating. However, we caution that most detection techniques rely on depthwise integration of a signal (e.g., fluorescence), which then scales as the channel height, h. Thus, TGF system designers must also optimize the channel width subject to their desired detection limits.

38.4.3 Isotachophoresis

38.4.3.1 Introduction

Isotachophoresis [68] is an electrophoretic preconcentration and separation technique that utilizes a heterogenous buffer system of disparate electrophoretic mobilities. Typically, a plug containing sample ions to be focused and separated is introduced between the leading and trailing electrolyte (LE and TE) whose mobilities are respectively higher and lower than any of the mobilities of sample ions. Under the influence of an electric field, the sample ions separate and redistribute themselves in contiguous zones in order of reducing mobility starting from LE to TE (each is focused into its respective, mobility-dependent focal point). At steady state, these focused sample zones migrate at a same speed as the leading zone, hence the name "iso-tacho-phoresis."

ITP, also known as displacement electrophoresis, was first performed in capillary tubes by Everaerts et al. [69] for the separation of strong anions using a thermocouple detector. Since then, ITP has been used for the analysis of various important chemical and biological species such as amino acids [70], peptides [71], nucleotides [72], proteins [73,74], heavy metal ions [75], and other organic/inorganic ions [76,77] on a variety of detection platforms such as UV absorbance, conductivity and fluorescence detection. Over the past 15 years, ITP has been used as a preconcentration technique in conjunction with CE [78]. This mode of ITP, referred to as transient isotachophoresis (tITP), has been implemented on microchip platform in the recent years to achieve improved sensitivity [22,79,80].

38.4.3.2 Basic Theory and Implementation

ITP leverages differences in the mobility of sample ions to create a segregation of species on the basis of mobility. ITP separation results in a system of contiguous sample zones, sandwiched between leading and trailing electrolytes, migrating at identical speeds. The inherent preconcentration effect of ITP maintains sharp concentration boundaries between adjacent sample zones. In the absence of dispersion due to (radially) nonuniform bulk flow, the thickness of these boundaries is governed by the balance of electromigration and diffusion flux, as we shall discuss later. Away from this diffused boundary region, the sample concentration is uniform and can be obtained in each zone using species conservation equations and the electroneutrality condition [81]. Consider a simple model ITP system, shown in Figure 38.13, consisting of a plug of sample ions (X_i) injected between the leading electrolyte (LE) and trailing electrolyte (TE), and common counterion (A) present everywhere. For now, we assume EOF is fully suppressed to negligible levels. After sufficient focusing time, the various zones in the system will develop locally uniform concentrations (concentration "plateaus" around their respective focal points) where diffusive fluxes are locally insignificant. For this long-time condition, the species conservation equations can be simplified to obtain the well-known Kohlrausch regulating function (KRF) [82] given by

$$\left(\sum_i \frac{C_i}{\mu_{\mathrm{eph},i}}\right)_x = f(x), \tag{38.42}$$

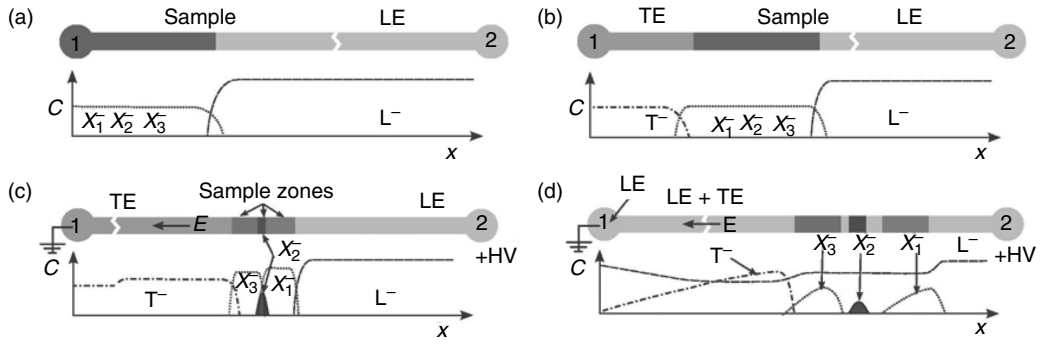

FIGURE 38.13 A schematic of the steps involved in a typical anionic ITP experiment is shown. (a) First, the capillary/microchannel is filled with the leading electrolyte using pressure driven flow. Sample electrolyte is introduced in well 1 and the capillary/channel is partially filled with this sample electrolyte by applying vacuum on well 2. (b) Well 1 is emptied and filled with the trailing electrolyte which is then drawn into the capillary/channel. (c) Next, high voltage is applied across the capillary and an electric field is setup inside the capillary/channel initiating separation of sample zones and achieving ITP condition. Sample ions X_1 and X_3 are present in high initial concentration and hence their zones form plateau shaped peaks and achieve the concentration as required by KRF. X_2 appears as a peak in the diffused interface between X_1 and X_3 zones and has a much lower concentration than predicted by KRF. (d) Finally, well 1 is emptied and is filled with LE. The LE ions overspeed the TE and sample ions and "break" the ITP mode into CE mode. The sample peaks separate in the CE mode and also disperse due to electromigration dispersion.

where C_i and $\mu_{\text{eph},i}$ are the concentration and the mobility of species i, at axial location x in the channel. The constant (in time) function $f(x)$ is governed by the initial condition. This relation can be stated as follows: The sum of concentration-to-mobility ratio of all species at a given location in the channel (relative to the channel wall at negligible electroosmosis conditions) remains invariant with time.

Using the KRF, we can arrive at the following expression to obtain the concentration adjustment of an ITP zone assuming no dispersions and bulk fluid velocity [83]:

$$C_X = C_L \frac{\mu_X}{\mu_L} \frac{\mu_A + |\mu_L|}{\mu_A + |\mu_X|}, \tag{38.43}$$

where the adjusted sample concentration, C_X, is strictly a function of the LE concentration and electrophoretic mobilities in the nondiffuse one-dimensional model. Note that KRF may be used to estimate sample concentration in an ITP zone only if the species are strong ions (fully ionized). Further, the species are present in sufficiently high initial concentration to form concentrated regions with finite-width, but locally uniform concentrations (a plateau in analyte peaks, e.g., samples X_1 and X_3 in Figure 38.13c).

For low initial concentrations (or short preconcentration times), the ITP zone width can be on the order of the diffusion width between zones (e.g., sample X_2 in Figure 38.13c). In that case, as pointed out by Svoboda [84], analyte width is a function of both initial concentration and injected plug length (see also the quantitative data of Jung et al. [22]). This regime of ITP has been called the spiked mode [85] and here, the analyte zone appears as a spike between adjacent zones rather than a plateau. One often encounters this spiked mode ITP in trace analyte detection and separation. In this regime, Taylor dispersion is a critical factor in determining the maximum concentration enhancement achieved. As a result, the sample peak widths (in spike mode) and interfaces between ITP zones can often be greater than peak widths predicted by diffusion alone. In our work, this factor is also reflected in the rate of growth of sample peaks. Despite this, there has been very little work in the analysis and modeling of Taylor dispersion in ITP.

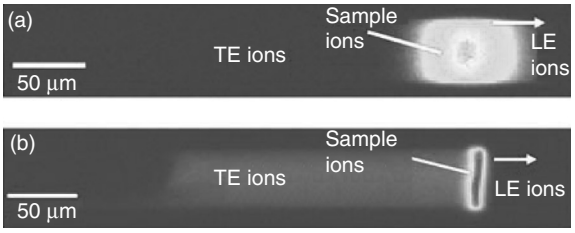

FIGURE 38.14 **(See color insert following page 810.)** CCD camera images of on-chip sample peaks of AlexaFluor 488 at the LE/TE interface in two different ITP experiments. In (a) there is finite (nonuniform) EOF and the sample peak streamwise dimension is on the order of channel width or larger. In (b) EOF is suppressed and the sample is concentrated in narrower zone (~5 μm) at relatively high electric field. While Taylor dispersion based analysis is probably applicable in the first case, more comprehensive modeling is required for case (b).

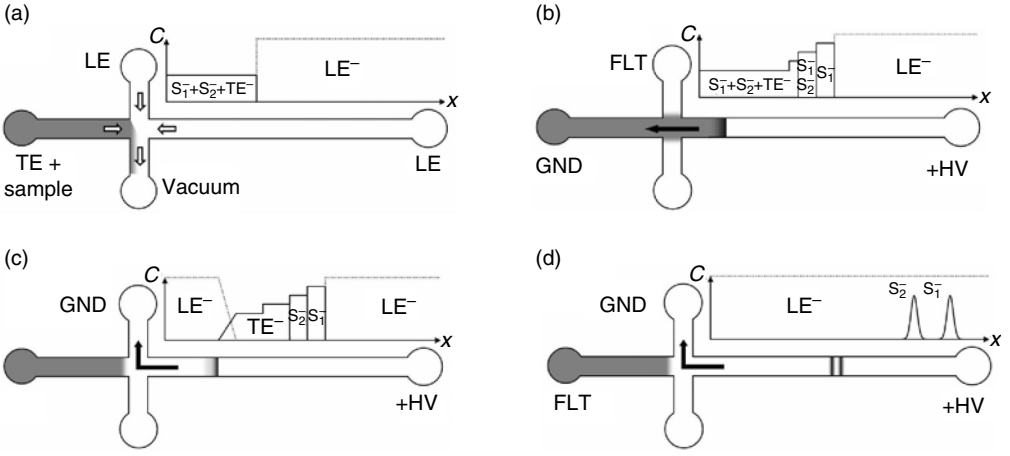

FIGURE 38.15 Schematic of ITP/CE assay protocol in a microchip. Configurations of co-ions are also shown at each step. (a) The north and the south reservoirs are filled LE, and the west reservoir is filled with a mixture of TE and sample. TE/LE boundary is formed by applying vacuum at the south reservoir. White arrows show the direction of pressure-driven flows. (b) ITP preconcentration is initiated by applying high voltage and ground at the east and west reservoirs, respectively. The black arrow denotes the direction of electric field. Sample anions electromigrate toward the anode as EOF is suppressed. The early stage of ITP preconcentration results in a partial separation (i.e., moving boundary electrophoresis). (c) The field is switched toward the north reservoir to inject LE ions behind the sample and initiate CE. ITP preconcentration continues until LE ions overtake the TE and sample ions. (d) Separation of samples occurs further downstream where sample ions electromigrate in nearly homogeneous LE electrolyte (remnant of TE not shown).

Example visualizations of ITP-focused sample peaks in a 50 μm wide by 20 μm deep (isotropically etched) microchannel are shown in Figure 38.14. The top image shows a typical ITP sample peak in a channel with finite EOF and Taylor dispersion. Interface lengths are on the order of or larger than the characteristic channel cross section dimensions. In this experiment, the ITP stacking occurs over a long duration (~5 min) such that the peak has a substantial axial dimension compared to the channel width and has clearly dispersed edges. The area-averaging dispersion analysis and scaling presented earlier should apply here. Figure 38.14b shows early stage of an ITP plug created on-chip with high-quality EOF suppression (using poly-*N*-hydroxyethylacrylamide [PHEA] coating on a borosilicate glass wall [22]), high electric field (~1000 V/cm in the TE), and high LE concentration (~1 M). The injection protocol used here is shown in Figure 38.15a,b. Here, the sample peak is a narrow concentration "shock wave" with extremely high electric field and concentration

gradients. Accurate prediction of the focusing dynamics of such a peak will probably require fairly comprehensive two- and three-dimensional models.

The coupling of ITP with CE is shown in Figures 38.13d and 38.15c–d. This coupling is referred to as transient ITP (tITP). tITP is typically achieved by replacing the TE ions with LE ions, which interrupts the ITP process. After sufficient sample preconcentration via ITP (as in Figure 38.13c), LE ions are introduced behind the contiguous sample zones. This is accomplished by either manually exchanging the buffer in well 1 (e.g., with a hand pipette, as shown in Figure 38.13c) or by using a side channel of a microchip to inject LE ions electrokinetically behind the train of sample zones (Figure 38.15c,d) [22,86]. The LE ions enter the sample zones faster. Sample zone concentrations reduce in order to satisfy the KRF-type regulation, and sample plug typically forms long tails as shown. This form of dispersion is termed as electromigration dispersion (EMD), and has been extensively investigated [87–89]. Once the ITP process is interrupted, the samples separate via standard mobility-based CE separation.

38.4.3.3 Dispersion Theory

The isotachophoretic boundary between two adjacent zones, under constant current condition and in the absence of bulk flow, assumes a constant width governed by the balance of electromigration and dispersion fluxes. For negligible electroosmosis (and negligible Taylor dispersion), the dispersion is determined by diffusion alone. Analytical solution to the concentration of the species in this diffused boundary, for a three-component fully ionized system, has been presented by Saville et al. [90]. The characteristic length-scale, δ, of the ITP boundary in this case is given by

$$\delta = \frac{\mu_L \mu_T}{\mu_L - \mu_T} \frac{C_L}{j} \left(\frac{k_B T}{e} \right), \tag{38.44}$$

where μ_L and μ_T are electrophoretic mobilities of LE and TE, respectively, C_L is the concentration of leading ion, j is the current density, and $k_B T/e$ is the thermal voltage. For negligible Taylor dispersion (e.g., low fields), peak axial dimension scales as D/E (since diffusivity is proportional to mobility by the Nernst–Einstein relation). Typical concentration profiles of LE, TE, and counterion in an ITP boundary (with molecular diffusion alone contributing to dispersion) are shown in Figure 38.16.

The case of nonsuppressed EOF conditions is much more complex. For even trace EOF mobilities, there will be a mismatch in electroosmotic mobility and electric field in the adjacent zones. This results in a mismatch in the electroosmotic velocity and hence generation of internal pressure gradients as discussed earlier. These pressure gradients result in increased width of the interface due to dispersion and have detrimental effects on preconcentration of trace samples via ITP.

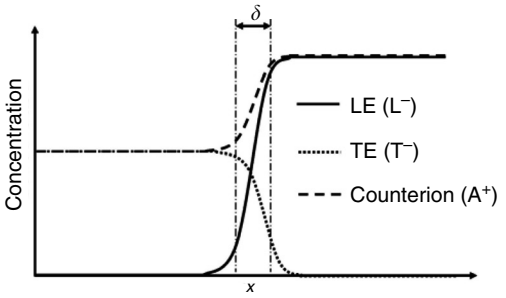

FIGURE 38.16 Schematic of the distribution of ions in the diffused interface between leading and trailing electrolyte in an ITP system. δ is the characteristic length scale of this diffused boundary, obtained from the balance of electromigration and diffusion fluxes.

Saville [91] investigates the effect of electroosmosis on the interface between two ITP zones. To our knowledge, this is the only published Taylor dispersion analysis for ITP. Saville's analysis is for a simplified problem. He neglects the influence of electrolyte concentration and pH on electroosmotic mobility. Similar to the analyses presented earlier, a purely axial flow velocity is split into the bulk area average velocity $\langle u \rangle$ and a deviation velocity, $u_p' = u - \langle u \rangle$. The pressure-driven flow velocity component due to a mismatch in electroosmotic slip velocity (alone) is $u_p' = 2(\mu_{\text{eof}} E - \{\mu_{\text{eof}} E\})(1 - 2r^2/a^2)$. While simplifying approximations, Saville assumes μ_{eof} is uniform, and the local electric field governing EOF (but not the electric field governing electrophoresis) is approximately uniform in x. For example, assuming the TE voltage drop is much larger than that of the LE; and assuming solute plug is approximately halfway along the length of the channel, our expression reduces to $\mu_{\text{eof}} E_{\text{TE}}(x)(1 - 2r^2/a^2)$. Saville writes this as

$$u_p' = \mu_{\text{eof}} E_0 (1 - 2r^2/a^2), \tag{38.45}$$

where E_0 is assumed constant and uniform. Saville further expands μ_{eof} as $-\varepsilon\zeta E/\eta$ (where ε is the permittivity, μ is the viscosity of the liquid, and ζ is the zeta potential) but we shall retain the more compact form here. In a frame of reference moving at $\langle u_{\text{bulk}} \rangle = U_{\text{EOF}} + U_p$, the species conservation equation for any species i can be expressed as

$$\frac{\partial C_i}{\partial t} + u_p' \frac{\partial C_i}{\partial x} = \frac{\partial}{\partial x}\left[-\mu_{\text{eph},i} C_i E_x(x,r) + D_i \frac{\partial C_i}{\partial x}\right] + \frac{1}{r}\frac{\partial}{\partial r} r\left[-\mu_{\text{eph},i} C_i E_r(x,r) + D_i \frac{\partial C_i}{\partial r}\right], \tag{38.46}$$

where $\mu_{\text{eph},i}$ is the electrophoretic mobility ($\text{m}^2/\text{V/s}$), E is the electric field (V/m), and C_i is the concentration of the species i. The species relations are constrained by the electroneutrality approximation expressed as

$$\sum_i z_i C_i = 0. \tag{38.47}$$

Next, the conservation equations are transformed to the frame of reference moving with the interface at the speed U_{ITP} ($U_{\text{ITP}} = \mu_{\text{L}} E_{\text{LE}}$, where E_{LE} is the electric field strength in the LE region) and subsequently nondimensionalized to obtain the following dimensionless equations:

$$\begin{aligned} &-C_i^* + Pe(1 - 2r^{*2})\frac{\partial C_i^*}{\partial x^*} \\ &\quad = \frac{\partial}{\partial x^*}\left[-\mu_{\text{eph},i}^* C_i^* E_x^* + \mu_{\text{eph},i}^* \frac{\partial C_i^*}{\partial x^*}\right] + \lambda^2 \frac{1}{r^*}\frac{\partial}{\partial r^*} r^*\left[-\mu_{\text{eph},i}^* C_i^* E_r^* + \mu_{\text{eph},i}^* \frac{\partial C_i^*}{\partial r^*}\right] \end{aligned} \tag{38.48}$$

and

$$\sum_i z_i C_i^* = 0. \tag{38.49}$$

In arriving at the previous equation, the following scaling has been used:

$$C_i^* = C_i/C_A, \quad \mu_{\text{eph},i}^* = \mu_{\text{eph},i}/\mu_{\text{eph},A}, \quad x^* = x/l, \quad r^* = r/a, \quad E_x^* = E_x \mu_{\text{eph},A} l/D_A$$

and

$$E_r^* = E_r \mu_{\text{eph},A} a/D_A.$$

Here, the following dimensionless parameters appear: Peclet number $Pe = \mu_{\text{eof}} E_0 l / D_A$ and the aspect ratio $\lambda = l^2/a^2$, where l is the electrical length scale obtained by balancing diffusion and electromigration flux, $l = D_A / U_{\text{ITP}}$.

The typical value of Peclet number is ~10 indicating that convection plays an important role in determining the shape of the interface. By performing asymptotic expansion on the concentration and potential terms in the species conservation equation and area-averaging the equation over the cross section of the capillary, Saville obtains the following:

$$-\frac{\partial \langle C_i^* \rangle}{\partial x^*} = \frac{\partial}{\partial x^*}[-\mu^*_{\text{eph},i} \langle C_i^* \rangle \langle E_x^* \rangle] + \left(\mu^*_{\text{eph},i} + \frac{(Pe)^2}{48 \mu^*_{\text{eph},i} \lambda^2} \right) \frac{\partial^2 \langle C_i^* \rangle}{\partial x^{*2}}. \tag{38.50}$$

Reverting back to dimensional form, we write

$$-U_{\text{ITP}} \frac{\partial \langle C_i \rangle}{\partial x} = \frac{\partial}{\partial x}[-\mu_{\text{eph},i} \langle C_i \rangle \langle E_x \rangle] + \left(D_i + \frac{(\mu_{\text{eof}} E_0)^2 a^2}{48 D_i} \right) \frac{\partial^2 \langle C_i \rangle}{\partial x^2}. \tag{38.51}$$

Hence, we arrive at a expression similar to the one derived in Taylor dispersion using area-averaging section, with

$$D_{\text{eff},i} = \left(D_i + \frac{(\mu_{\text{eof}} E_0)^2 a^2}{48 D_i} \right).$$

Note that Equation 38.49 follows from our more general Equation 38.16 (e.g., transform the equation to the U_{ITP} frame of reference and assume a uniform constant value of D_{eff}). Saville presents numerical solutions of his model for the case where $\lambda = 1$, $\mu^*_{\text{eph,LE}} = 1$, $\mu^*_{\text{eph,TE}} = 0.5$, and $Pe = 10$. The model shows interface width (e.g., the interface between two adjacent species) as a strong function of Pe (and E_0). In the conditions Saville modeled, Taylor dispersion increases the effective dispersion coefficient up to ~18-fold over diffusion alone.

Despite the dearth of work on ITP Taylor dispersion, there is fairly clear experimental evidence that Taylor dispersion often limits maximum achievable concentration increase. Next, we present experimental studies of Taylor dispersion in ITP and present an empirical optimization of ITP that minimizes dispersion to maximize preconcentration factor. We studied the effects of Taylor dispersion on the width of single interface ITP systems shown schematically in Figure 38.15a-b, under constant (in time) current conditions. In a typical ITP experiment, the LE contains high concentration of Cl^- (100 mM to 1 M), the TE contains $HEPES^-$ (5–100 mM) and the sample ions (Alexa Fluor 488) in trace concentration (100 aM to 1 nM). We setup an interface between the LE and TE using pressure-driven flow, and ITP is initiated by applying high voltage (~3 kV) across this interface. Under the influence of the applied electric field, sample ions overspeed TE ions in the TE zone and stack at the LE/TE interface. Figure 38.17 shows a typical result for the width (along the axial direction) of the focused sample plug as it propagates down the channel toward the anode. Data are shown for four values of applied current in this 50 μm wide by 20 μm deep borosilicate glass microchannel (Mycralyne Inc.). Here, EOF was suppressed by adding polyvinyl pyrrolidone (PVP) (0.2% w/w) to the LE and TE. In the absence of Taylor dispersion (but including the effects of diffusion), we expect the sample plug width to remain constant. However, the sample width clearly grows nearly linearly in space. This behavior of sample plug width is observed even in ITP experiments with high degree of EOF suppression. We hypothesize that this type of growth is due to a mismatch in the EOF between the LE and TE region, which induces Taylor dispersion. This experimental evidence suggests that the interface dimension in ITP is often controlled by Taylor dispersion.

Analytical and even numerical computations of ITP processes including diffusion and Taylor dispersion are difficult. However, the analyses presented in this chapter can be used as a guide for

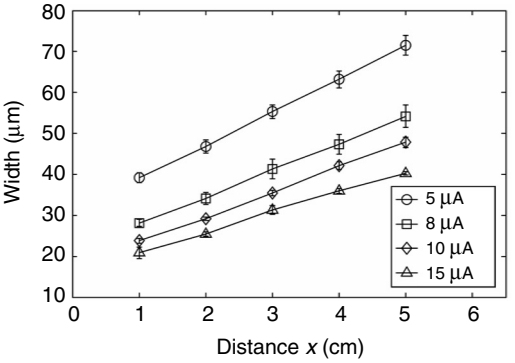

FIGURE 38.17 Plot of the width of the sample plug (10 nM Alexa Fluor 488) focused at the interface of LE (750 mM Tris–Hcl) and TE (25 mM Tris-Hepes) at various locations downstream in a 50 μm wide (20 μm deep) microchannel. Each data set represents five realizations of a constant current ITP experiment.

empirical optimizations of the ITP process. Key parameters influencing the sample preconcentration achieved are the concentrations of LE, TE, and the initial sample concentration; the local applied electric field; the initial conductivity gradient of the initial condition, which partly determines time to reach steady state; and the degree to which EOF is suppressed.

Jung et al. [22] performed a systematic variation of LE, TE, and sample concentration and measured the effect of these variations on concentration increase, CI (CI = $C_{\text{sample,final}}/C_{\text{sample}}$). In each case, we ensure that the ITP zones reached a fully preconcentrated state (i.e., maximum focusing) by verifying the transients of the preconcentration procedure using full-field imaging at low magnifications. In all cases, ITP zones reached a quasi-steady concentration, but we emphasize this does not imply that the KRF analysis is valid (since plateau-shaped peaks were not achieved [84]). We suppressed EOF (to minimize Taylor dispersion) by adding 0.1% (w/w) poly-*N*-hydroxyethylacrylamide (PHEA) to all electrolytes to suppress EOF. We tried several suppression strategies including poly-ethyPEO coating and PVP, but PHEA yielded the lowest electroosmotic mobility (as verified by current monitoring measurements [23]). For convenience in working with relatively high voltages (up to 3 kV), we used constant voltage control in this optimization of preconcentration.

Effects of LE (NaCl) concentration, C_{LE}, TE (HEPES) concentration, C_{TE} and initial concentration of sample (Alexa Fluor 488), $C_{\text{S,initial}}$ on sample preconcentration are summarized in Figure 38.18. C_{LE} was varied from 10 mM to 1 M to study its effect on maximum focused sample concentration, $C_{\text{S,final}}$ and concentration increase, CI (Figure 38.18a). The 5 mM HEPES TE solution contained 1 nM Alexa Fluor 488 as a sample. The focused sample concentration is nearly directly proportional to the concentration of LE, as expected from a one-dimensional nondispersive model (i.e., KRF theory). However, the nondispersive model drastically underpredicts the proportionality constant; the measured focused sample concentrations are 3500- to 7900-fold less than that predicted by Equation 38.43 despite all cases reaching fully-focused state. This gross difference between KRF theory and experiments is because the sample is in a "smeared" region of locally varying conductivity and electric field, as dictated by the effects of diffusion and Taylor dispersion.

Figure 38.18a also shows the effect of C_{TE} on ITP preconcentration, where C_{TE} were varied from 1 to 100 mM. The LE was fixed at 1 M NaCl, and $C_{S,\text{initial}}$ was fixed at 1 nM. The KRF model suggests that focused sample concentration is not a function of $C_{S,\text{initial}}$ or C_{TE}. However, the measurements show that $C_{S,\text{final}}$ increased for lower C_{TE} (i.e., as conductivity ratio increases). High LE-to-TE conductivity ratios (associated with low TE concentrations) increase the electric fields in the TE and focused sample zones. High electric field leads to fast-focusing dynamics and high electric Peclet numbers ($U_{\text{eph}}a/D$, where a is the characteristic channel scale) and thereby, high $C_{S,\text{final}}$, as the preconcentration process is less susceptible to dispersion. Higher electric fields would

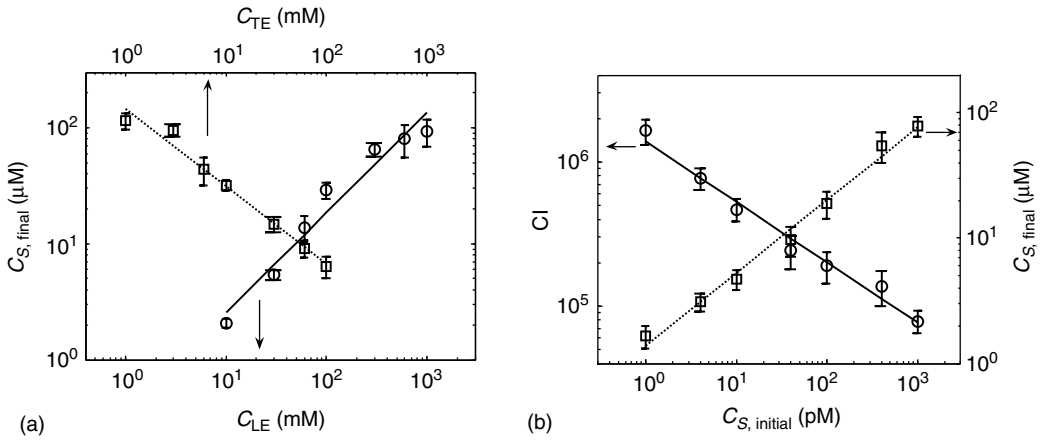

FIGURE 38.18 Parametric variations of initial concentration profile. The nominal applied field was 220 V/cm. CCD viewing area was centered 30 mm downstream of the channel intersection. (a) Maximum focused sample concentration, $C_{S,\text{final}}$, versus LE concentration, C_{LE} and TE concentration, C_{TE}. For variation of C_{LE}, sample analyte and TE were respectively 1 nM alexa fluor 488 and 5 mM HEPES. The regression coefficient, R^2, is 0.95. For variation of C_{TE}, sample analyte and LE were respectively 1 nM alexa fluor 488 and 1 M NaCl. $R^2 = 0.97$. (b) CI and $C_{S,\text{final}}$ versus initial sample concentration, $C_{S,\text{initial}}$. TE and LE were 5 mM HEPES and 1 M NaCl, respectively. The regression coefficients for CI and $C_{S,\text{final}}$ are respectively 0.97 and 0.98.

eventually lower maximum focusing due to the effects of dispersion (e.g., due to Taylor dispersion or Joule heating or both).

Next, initial sample concentrations, $C_{S,\text{initial}}$ were varied from 1 pM to 1 nM as shown in Figure 38.18b. The LE and TE were, respectively, fixed at 1 M NaCl and 5 mM HEPES. The LE-to-TE conductivity ratio was kept constant at 1.3×10^3 in an effort to decouple the dependence of the TE zone electric field on this conductivity ratio. The data shows CI increases as $C_{S,\text{initial}}$ decreases. This trend is roughly consistent with the KRF model. However, the dependence of CI on $C_{S,\text{initial}}$ is weaker than the inversely proportional dependence predicted by the simple model (CI changes just under two orders of magnitude while $C_{S,\text{initial}}$ changes three orders of magnitude). This discrepancy is also apparent in the measurements of the maximum concentration, $C_{S,\text{final}}$. The experimental data show $C_{S,\text{final}}$ as a linear function of (although not directly proportional to) $C_{S,\text{initial}}$, which is not attributable to changes in local field in the TE zone. We again hypothesize that this discrepancy between the simple model and observations is due directly to the effects of dispersion. Dispersed interfaces of finite width cause a final sample concentration to be a function of initial sample concentration.

38.4.3.4 Performance and Guidelines

These experimental parametric studies yield important insight into key ITP stacking parameters and suggest strategies for optimizing ITP in practice. Suppression of EOF to minimize Taylor dispersion is a key component. Also important are high LE concentration and low initial sample concentration to maximize achievable concentration increase, and the implementation of a single-column ITP configuration (where initially, there is a single interface between the LE and the TE/sample mixture) to inject a large effective sample width. As shown in Figure 38.18b, these simple strategies derived from earlier scaling arguments achieve ITP preconcentration with final-to-initial sample concentration ratios exceeding one million.

An example implementation of these strategies is shown in Figure 38.19. These are results of a tITP assay (again, ITP followed by injection of LE ions on the cathode side of the TE to interrupt ITP and initiate CE), which uses the single interface ITP configuration described schematically in Figure 38.15. The figure shows two example separations of 100 aM (100 attomolar) concentrations

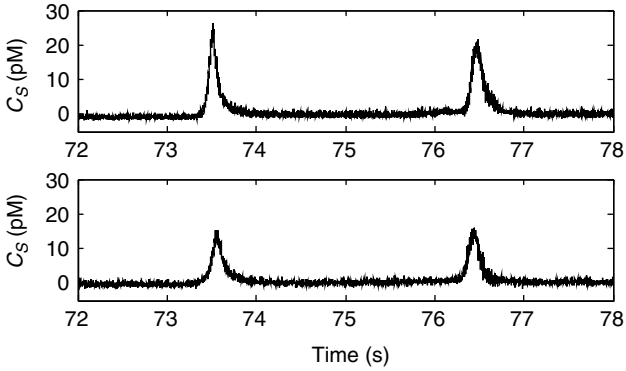

FIGURE 38.19 Two 100 aM sample electropherograms of ITP/CE separation of Alexa Fluor 488 (the peaks near 73.5 s) and Bodipy (peaks near 76.5 s). A glass microchip (microchannel cross-sectional dimensions are 50 μm wide and 20 μm deep) and 60× water immersion objective (N.A. = 0.9) were used. The detector was located 30 mm downstream of the injection region.

each of Alexa Fluor 488 and Bodipy, detected 30 mm after injection with 40 s ITP preconcentration under a nominal field of 220 V/cm. LE and TE were 600 mM NaCl and 5 mM HEPES, respectively. The concentrations measured after injection, ITP preconcentration, and separation are, respectively, 21 and 16 pM for Alexa Fluor 488 and bodipy, as averaged across five realizations. This experiment achieves a concentration increase of 2.1×10^5 fold relative to the initial sample concentration of 100 aM. This 100 aM sensitivity is, to our knowledge, the highest ever reported sensitivity for an electrophoresis experiment.

38.5 CONCLUDING REMARKS

Dispersion effects arising from nonuniform fluid motion have detrimental effects on CE sensitivity and resolution. Quantification and minimization of dispersion effects is especially important for sample stacking and focusing techniques. In preconcentration methods, EOF of heterogeneous buffer systems give rise to internal pressure gradients and strong dispersive forces. Generalized Taylor dispersion analysis is a powerful approach for quantifying these effects. More importantly, scaling, analytical solutions, and numerical solutions of Taylor dispersion provide unique insight. This can guide the choices of separation voltage, EOF suppression strategy, and channel shape, width, and depth for a given target analyte and buffer chemistry. The goal of such models and understanding is the optimization of preconcentration efficiency and resolution across a broad range of physical regimes and techniques.

Further improvements in the predictive capability of the stacking and focusing models presented here can be made by accounting for the 3D effects of typical D-shaped, wet-etched channel cross sections. More sophisticated dispersion analyses of the unsteady three-dimensional velocity field should also be carried out. This is particularly important for the high electric field regimes of TGF and ITP, where the sample plug widths become on the order of, or smaller than, the channel width. More comprehensive models should aid in the systematic design and optimization of CE separations under a wide range of conditions.

REFERENCES

1. Vlastimil Hruska, M.J., Bohuslav Gas, Simul 5—Free dynamic simulator of electrophoresis. *Electrophoresis*, 2006, 27: 984–991.

2. Taylor, G., Dispersion of soluble matter in solvent flowing slowly through a tube. *Proc. Roy. Soc. A*, 1953, 225: 186–203.
3. Bharadwaj, R., Santiago, J.G., and Mohammadi, B., Design and optimization of on-chip capillary electrophoresis. *Electrophoresis*, 2002, 23: 2729–2744.
4. Bharadwaj, R. and Santiago, J.G., Dynamics of field-amplified sample stacking. *J. Fluid Mech.*, 2005, 543: 57–92.
5. Aris, R., On the dispersion of a solute in a fluid flowing through a tube. *Proc. Roy. Soc. London, Ser. A*, 1956, 235: 67–77.
6. Dutta, D. and Leighton, D.T., Dispersion reduction in pressure-driven flow through microetched channels. *Anal. Chem.*, 2001, 73: 504–513.
7. Brenner, H., A general theory of Taylor dispersion phenomena. *PCH PhysicoChem. Hydrodyn.*, 1980, 1: 91–123.
8. Stone, H.A. and Brenner, H., Dispersion in flows with streamwise variations of mean velocity: Radial flow. *Ind. Eng. Chem. Res.*, 1999, 38: 851–854.
9. Griffiths, S.K. and Nilson, R.H., Hydrodynamic dispersion of a neutral nonreacting solute in electroosmotic flow. *Anal. Chem.*, 1999, 71: 5522–5529.
10. Pennathur, S. and Santiago, J.G., Electrokinetic transport in nanochannels. 1. Theory. *Anal. Chem.*, 2005, 77: 6772–6781.
11. Griffiths, S.K. and Nilson, R.H., Charged species transport, separation, and dispersion in nanoscale channels: Autogenous electric field-flow fractionation. *Anal. Chem.*, 2006, 78: 8134–8141.
12. Probstein, R.F., *Physicochemical Hydrodynamics: An Introduction*, 2nd ed. 1994, New York: John Wiley & Sons, p. 400.
13. Lin, H., Storey, B.D., Oddy, M.H., Chen, C.-H., and Santiago, J.G., Instability of electrokinetic microchannel flows with conductivity gradients. *Phys. Fluids*, 2003, 16: 1922–1935.
14. Chen, C.H., et al., Convective and absolute electrokinetic instability with conductivity gradients. *J. Fluid Mech.*, 2005, 524: 263–303.
15. Deen, W.M., *Analysis of Transport Phenomena*. 1998, New York: Oxford University Press.
16. Santiago, J., Electroosmotic flows in microchannels with finite inertial and pressure forces. *Anal. Chem.*, 2001, 73: 2353–2365.
17. Storey, B.D., et al., Electrokinetic instabilities in thin microchannels. *Phys. Fluids*, 2005, 17: 1922–1935.
18. Lin, H., et al., Instability of electrokinetic microchannel flows with conductivity gradients. *Phys. Fluids*, 2004, 16: 1922–1935.
19. Gas, B. and Kenndler, E., Dispersive phenomena in electromigration separation methods. *Electrophoresis*, 2000, 21: 3888–3897.
20. Ajdari, A., Bontoux, N., and Stone, H.A., Hydrodynamic dispersion in shallow microchannels: The effect of cross-sectional shape. *Anal. Chem.*, 2006, 78: 387–392.
21. Anderson, J.L. and Idol, W.K., Electroosmosis through pores with nonuniformly charged walls. *Chem. Eng. Comm.*, 1985, 38: 93–106.
22. Jung, B., Bharadwaj, R., and Santiago, J.G., On-chip million fold sample stacking using single interface isotachophoresis. *Anal. Chem.*, 2006, 78: 2319–2327.
23. Huang, X.H., Gordon, M.J., and Zare, R.N., Current-monitoring method for measuring the electroosmotic flow-rate in capillary zone electrophoresis. *Anal. Chem.*, 1988, 60: 1837–1838.
24. Santiago, J.G., Wereley, S.T., Meinhart, C.D., Beebee, D.J., and Adrian, R.J., A particle image velocimetry system for microfluidics. *Exp. Fluids*, 1998, 25: 316–319.
25. Devasenathipathy, S. and Santiago, J.G., Electrokinetic flow diagnostics, in *Micro- and Nano-Scale Diagnostic Techniques*. 2002, Ed. K.S. Breuer, New York: Springer Verlag.
26. Probstein, R.F., *Physicochemical Hydrodynamics*. 1994, New York: John Wiley & Sons.
27. Hunter, R.J., *Zeta Potential in Colloid Science*. 1981, London: Academic Press.
28. Kirby, B.J. and Hasselbrink, E.F., Zeta potential of microfluidic substrates: 2. Data for polymers. *Electrophoresis*, 2004, 25: 203–213.
29. Kirby, B.J. and Hasselbrink, E.F., Zeta potential of microfluidic substrates: 1. Theory, experimental techniques, and effects on separations. *Electrophoresis*, 2004, 25: 187–202.
30. Yao, S., et al., Porous glass electroosmotic pumps: Design and experiments. *J. Coll. Interf. Sci.*, 2003, 268: 143–153.

31. Burgi, D.S. and Chien, R.L., Optimization of sample stacking for high performance capillary electrophoresis. *Anal. Chem.*, 1991, 63: 2042–2047.
32. Xuan, X.C. and Li, D.Q., Analytical study of Joule heating effects on electrokinetic transportation in capillary electrophoresis. *J. Chromatogr. A*, 2005, 1064: 227–237.
33. Tang, G.Y., et al., Modeling of electroosmotic flow and capillary electrophoresis with the joule heating effect: The Nernst–Planck equation versus the Boltzmann distribution. *Langmuir*, 2003, 19: 10975–10984.
34. Burgi, D.S., Large-volume stacking of anions in capillary electrophoresis using an electroosmotic flow modifier as a pump. *Anal. Chem.*, 1993, 65: 3726–3729.
35. Burgi, D.S. and Chien, R.L., Optimization in sample stacking for high-performance capillary electrophoresis. *Anal. Chem.*, 1991, 63: 2042–2047.
36. Chien, R.L. and Burgi, D.S., Field amplified sample injection in high-performance capillary electrophoresis. *J. Chromatogr.*, 1991, 559: 141–152.
37. Chien, R.L. and Burgi, D.S., Field amplified polarity-switching sample injection in high-performance capillary electrophoresis. *J. Chromatogr.*, 1991, 559: 153–161.
38. Chien, R.L. and Burgi, D.S., Sample stacking of an extremely large injection volume in high-performance capillary electrophoresis. *Anal. Chem.*, 1992, 64: 1046–1050.
39. Chien, R.L., Sample stacking revisted: A personal perspective. *Electrophoresis*, 2003, 24: 486–497.
40. Chien, R.L. and Burgi, D.S., Field amplified sample injection in high-performance capillary electrophoresis. *J. Chromatogr.*, 1991, 559: 141–152.
41. Chien, R.L. and Burgi, D.S. On-column sample concentration using field amplification in CZE. *Anal. Chem.*, 1992, 64: A489–A496.
42. Jung, B., Bharadwaj, R., and Santiago, J.G., Thousand-fold signal increase using field amplified sample stacking for on-chip electrophoresis. *Electrophoresis*, 2003, 24: 3476–3483.
43. Jacobson, S. and Ramsey, J. Microchip electrophoresis with sample stacking. *Electrophoresis*, 1995, 16: 481–486.
44. Chien, R.L., Mathematical modeling of field amplified sample injection in high performance capillary electrophoresis. *Anal. Chem.*, 1991, 63: 2866–2869.
45. Zhang, C.X. and Thormann, W., Head-column field-amplified sample stacking in binary system capillary electrophoresis. 2. Optimization with a preinjection plug and application to micelllar electrokinetic chromatography. *Anal. Chem.*, 1998, 70: 540–548.
46. Jacobson, S.C., Ermakov, S.V., and Ramsey, J.M., Minimizing the number of voltage sources and fluid reservoirs for electrokinetic valving in microfluidic devices. *Anal. Chem.*, 1999, 71: 3273–3276.
47. Jacobson, S.C., et al., High-speed separations on a microchip. *Anal. Chem.*, 1994, 66: 1114–1118.
48. Jacobson, S.C., et al., Effects of injection schemes and column geometry on the performance of microchip electrophoresis devices. *Anal. Chem.*, 1994, 66: 1107–1113.
49. Grushka, E., McCormick, R.M., and Kirkland, J.J., Effect of temperature-gradients on the efficiency of capillary zone electrophoresis separations. *Anal. Chem.*, 1989, 61: 241–246.
50. Kirby, B.J., Zeta potential of microfluidic substrates: 1. Theory, experimental techniques, and effects on separations. *Electrophoresis*, 2004, 25: 187–202.
51. Yao, S., Hertzog, D.E., Zeng, S., Mikkelsen, J.C., and Santiago, J.G., Porous glass electroosmotic pumps: Design and experiments. *J. Coll. Interf. Sci.*, 2003, 268: 143–153.
52. Preisler, J. and Yeung, E.S., Characterization of nonbonded poly(ethylene oxide) coating for capillary electrophoresis via continuous monitoring of electroosmotic flow. *Anal. Chem.*, 1996, 68: 2885–2889.
53. Hjerten, S. and Zhu, M.D., Adaptation of the equipment for high-performance electrophoresis to isoelectric-focusing. *J. Chromatogr.*, 1985, 346: 265–270.
54. Righetti, P.G., *Isoelectric Focusing: Theory, Methodology, and Applications*, 1st ed. 1983, New York: Amsterdam, xv, 386 pages.
55. Herr, A.E., et al., On-chip coupling of isoelectric focusing and free solution electrophoresis for multidimensional separations. *Anal. Chem.*, 2003, 75: 1180–1187.
56. Ross, D. and Locascio, L.E., Microfluidic temperature gradient focusing. *Anal. Chem.*, 2002, 74: 2556–2564.
57. Balss, K.M., et al., DNA hybridization assays using temperature gradient focusing and peptide nucleic acids. *J. Am. Chem. Soc.*, 2004, 126: 13474–13479.

58. Balss, K.M., et al., Simultaneous concentration and separation of enantiomers with chiral temperature gradient focusing. *Anal. Chem.*, 2004, 76: 7243–7249.
59. Balss, K.M., et al., Micellar affinity gradient focusing: A new method for electrokinetic focusing. *J. Am. Chem. Soc.*, 2004, 126: 1936–1937.
60. Kamande, M.W., et al., Simultaneous concentration and separation of coumarins using a molecular micelle in micellar affinity gradient focusing. *Anal. Chem*., 2007, 79: 1791–1796.
61. Ghosal, S., Electrokinetic flow and dispersion in capillary electrophoresis. *Annu. Rev. Fluid Mech.,* 2006, 38: 309–338.
62. Huber, D.E. and Santiago, J.G., Taylor-Aris dispersion in temperature gradient focusing. *Electrophoresis*, 2007, 28: 2333–2344.
63. Kim, S.M., et al., Low-power concentration and separation using temperature gradient focusing via Joule heating. *Anal. Chem*., 2006, 78: 8028–8035.
64. Van Milligen, B.P., et al., On the applicability of Fick's law to diffusion in inhomogeneous systems. *Eur. J. Phys.*, 2005, 26: 913–925.
65. Ghosal, S., Lubrication theory for electro-osmotic flow in a microfluidic channel of slowly varying cross-section and wall charge. *J. Fluid Mech.*, 2002, 459: 103–128.
66. Huber, D.E., *Transport and Dispersion in Microfluidic Temperature Gradient Focusing*, Ph.D Thesis, 2006, Stanford University.
67. Hoebel, S.J., et al., Scanning temperature gradient focusing. *Anal. Chem.*, 2006, 78: 7186–7190.
68. Everaerts, F.M., Beckers, J.L., and Verheggen, T.P.E.M., *Isotachophoresis: Theory, Instrumentation, and Applications*. 1976, New York: Amsterdam.
69. Martin, A.J.P. and Everaert, F.M., Displacement electrophoresis. *Anal. Chim. Acta*, 1967, 38: 233.
70. Everaerts, F.M. and Van der Put, A.J.M., Isotachophoresis—Separation of amino acids. *J. Chromatogr.*, 1970, 52: 415.
71. Holloway, C.J. and Pingoud, V., The analysis of amino acids and peptides by isotachophoresis. *Electrophoresis*, 1981, 2: 127–134.
72. Bruchelt, G.G., Niethammer, D.D., and Schmidt, K.K.H., Isotachophoresis of nucleic acid constituents. *J. Chromatogr.*, 1993, 618: 57–77.
73. Delmotte, P., Analysis of complex protein mixtures by capillary isotachophoresis. *Sci. Tools*, 1977, 24: 33.
74. Schmitz, G. and Möllers, C., Analysis of lipoproteins with analytical capillary isotachophoresis. *Electrophoresis*, 1994, 15: 31–39.
75. Everaerts, F.M., et al., Determination of heavy metals by isotachophoresis. *J. Chromatogr. A*, 1985, 320: 263–268.
76. Sollenberg, J., Analytical isotachophoresis in biological monitoring of exposure to industrial chemicals. *J. Chromatogr. A*, 1991, 545: 369–374.
77. Gebauer, P. and Bocek, P., Recent progress in capillary isotachophoresis. *Electrophoresis*, 2000, 21: 3898–3904.
78. Krivankova, L., Gebauer, P., and Bocek, P., Some practical aspects of utilizing the online combination of isotachophoresis and capillary zone electrophoresis. *J. Chromatogr. A*, 1995, 716: 35–48.
79. Wainright, A., et al., Sample preconcentration by isotachophoresis in microfluidic devices. *J. Chromatogr. A*, 2002, 979: 69–80.
80. Xu, Z.Q., et al., Performance of electrokinetic supercharging for high-sensitivity detection of DNA fragments in chip gel electrophoresis. *Electrophoresis*, 2004, 25: 3875–3881.
81. Mosher, R.A., Saville, D.A., and Thormann, W., *The Dynamics of Electrophoresis*. 1992: VCH Weinheim New York.
82. Kohlrausch, F., Ueber concentrations-Verschiebungen durch Electrolyse in Inneren Von Losungen and losungsgemischen. *Ann. Phys. (Leipzig)*, 1897, 62: 209–239.
83. Martin, A.J.P. and Everaert, F.M., Displacement electrophoresis. *Proc. Roy. Soc. Lond. Ser. A—Math. Phys. Sci.*, 1970, 316: 493.
84. Svoboda, M. and Vacik J., Capillary electrophoresis with ultra violet detection some quantitative aspects, *Journal of Chromatography A,* 1976, 119: 539–547.
85. Nagyova, I. and Kaniansky, D., Discrete spacers for photometric characterization of humic acids separated by capillary isotachophoresis. *J. Chromatogr. A*, 2001, 916: 191–200.

86. Wainright, A., et al., Preconcentration and separation of double-stranded DNA fragments by electrophoresis in plastic microfluidic devices. *Electrophoresis*, 2003, 24: 3784–3792.
87. Thormann, W., Description and detection of moving sample zones in zone electrophoresis: Zone spreading due to the sample as a necessary discontinuous element. *Electrophoresis*, 1983, 4: 383–390.
88. Beckers, J.L., Steady-state models in electrophoresis: From isotachophoresis to capillary zone electrophoresis. *Electrophoresis*, 1995, 16: 1987–1998.
89. Hjertén, S.S., Zone broadening in electrophoresis with special reference to high-performance electrophoresis in capillaries: An interplay between theory and practice. *Electrophoresis*, 1990, 11: 665–690.
90. Saville, D.A. and Palusinski, O.A., Theory of electrophoretic separations. 1. Formulation of a mathematical-model. *Aiche J.*, 1986, 32: 207–214.
91. Saville, D.A., The effects of electroosmosis on the structure of isotachophoresis boundaries. *Electrophoresis*, 1990, 11: 899–902.